

Accepted Manuscript

The potential of phosphorus in clinopyroxene as a geospeedometer: examples from mantle xenoliths

I. Baziotis, S. Xydous, PD. Asimow, C. Mavrogonatos, S. Fliemetakis, S. Klemme, J. Berndt

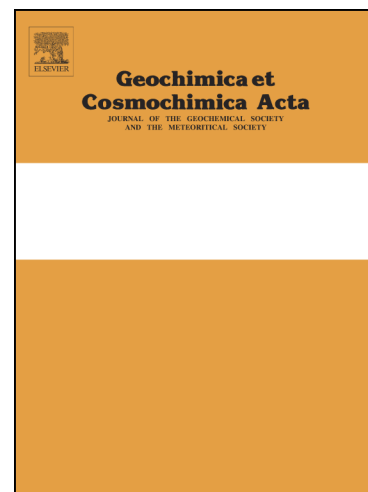
PII: S0016-7037(19)30250-9
DOI: <https://doi.org/10.1016/j.gca.2019.04.024>
Reference: GCA 11219

To appear in: *Geochimica et Cosmochimica Acta*

Received Date: 8 December 2018
Revised Date: 24 April 2019
Accepted Date: 24 April 2019

Please cite this article as: Baziotis, I., Xydous, S., Asimow, PD., Mavrogonatos, C., Fliemetakis, S., Klemme, S., Berndt, J., The potential of phosphorus in clinopyroxene as a geospeedometer: examples from mantle xenoliths, *Geochimica et Cosmochimica Acta* (2019), doi: <https://doi.org/10.1016/j.gca.2019.04.024>

This is a PDF file of an unedited manuscript that has been accepted for publication. As a service to our customers we are providing this early version of the manuscript. The manuscript will undergo copyediting, typesetting, and review of the resulting proof before it is published in its final form. Please note that during the production process errors may be discovered which could affect the content, and all legal disclaimers that apply to the journal pertain.



The potential of phosphorus in clinopyroxene as a geospeedometer: examples from mantle xenoliths

Baziotis, I.^{1*}, Xydous, S.¹, Asimow, P. D.², Mavrogonatos, C.³, Flemetakis, S.⁴, Klemme, S.⁴, Berndt, J.⁴

¹Agricultural University of Athens, Mineral Resources and Agricultural Engineering, Iera Odos str. 75, 11855 Athens, Greece, ²California Institute of Technology, Division of Geological and Planetary Sciences, Pasadena, California, 91125, USA, ³National and Kapodistrian University of Athens, Department of Geology and Geoenvironment, University Campus, Zografou, Athens, Greece, ⁴Westfälische Wilhelms-Univ. Münster, Institut für Mineralogie, Correnstrasse 24, Münster, Germany

*Corresponding author. Telephone: +30-2105294155. E-mail: ibaziotis@aua.gr

ABSTRACT

We investigate the potential to use concentrations and zoning patterns of phosphorus (P) in clinopyroxene as indicators of the rates of igneous and metasomatic processes, comparable to recent applications of P in olivine but applicable to more evolved rocks and lower temperatures of crystallization. Few high-P pyroxenes have been previously reported, and none have been analyzed in detail for the mechanism of P enrichment or the implications for mineral growth kinetics. Here, we report the discovery and characteristics of exotic phosphorus-rich secondary clinopyroxene in glassy pockets and veins in composite mantle xenoliths from the Cima Volcanic Field (California, USA) and the Middle Atlas Mountains (Morocco, West Africa). These glass-bearing xenoliths preserve evidence of melt infiltration events and the contrasting behavior of P in their pyroxene crystals constrains the different rates of reaction and extents of equilibration that characterized infiltration in each setting. We report optical petrography and chemical analysis of glasses and minerals for major elements by electron microprobe microanalyzer and trace elements by laser-ablation Inductively Coupled Plasma Mass Spectrometry. The Cima Volcanic Field specimen shows one end-member behavior, with unzoned P-rich clinopyroxene in a melt pocket. We attribute this occurrence to a slow crystallization process that occurred after the melt temperature reached near-equilibrium with the host rock and during which the P concentration in the melt was buffered by apatite saturation. In the Morocco xenolith, by contrast, clinopyroxene exhibits zonation with P increasing all the way to the rim, in contact with the glass. We ascribe this feature to a rapid growth process in which excess P was incorporated into the growing clinopyroxene from a diffusive boundary

layer. We demonstrate quantitative agreement between the enrichment of P and other trace elements and their expected diffusion and partitioning behavior during rapid growth. We suggest that P has not been widely reported in clinopyroxene in large part because it has rarely been looked for and that its analysis offers considerable promise as a kinetic indicator both in xenoliths and volcanic rocks.

Keywords: phosphorus content; phosphorus-rich pyroxene; diffusive relaxation; mantle xenolith; metasomatism

INTRODUCTION

Over the last decade or so, geochemists have increasingly sought to place robust constraints on the rates of magmatic processes (Demouchy et al., 2006, 2015; Peslier et al., 2008; Hilchie et al., 2014; Peslier and Bizimis, 2014; Warren and Hauri, 2014). One particularly promising element for preserving records of rate-dependent processes is phosphorus (P; note that we will not use the symbol P for pressure in this work, so “high-P” always means elevated phosphorus content rather than elevated pressure), a slowly-diffusing and moderately incompatible element (Tropper et al., 2004; Spandler et al., 2007; Boesenberg et al., 2012; Schneider et al., 2013; Elardo and Shearer, 2014; Ennis and McSween, 2014). Phosphorus content in olivine captures mineral growth histories and is then difficult to modify, even at magmatic temperatures over timescales of hundreds or thousands of years (e.g., Boesenberg and Hewins, 2010; Foley et al., 2013). The P^{5+} ion can substitute for Si^{4+} , with a variety of charge-compensating mechanisms, and substantial concentrations have been well-documented in olivine from many rock types, including mantle-derived xenoliths, komatiites, basalts with or without alkaline affinities, andesites, syenites, dacites, troctolites, and various meteorite classes (Agrell et al., 1998; Milman-Barris et al., 2008; Sakyi et al., 2012; Tschegg et al., 2010; Welsch et al., 2013, 2014, Welsch et al., 2016; Maisonneuve et al., 2016). In principle, the crystal chemistry of pyroxene should allow a variety of substitution mechanisms to accommodate phosphorus. However, available data suggest that P is quite incompatible in clinopyroxene, with most experimental partition coefficient values around 0.025, and are even more incompatible (partition coefficients 3 to 9 times lower) in orthopyroxene (data retrieved from Geochemical Earth Reference Model-GERM; Adam and Green, 2006; Brunet and Chazot, 2001).

Phosphorus enrichment in igneous olivine has been widely reported in recent years and applied to the interpretation of mineral growth kinetics. Phosphorus-rich zones in olivine have generally been attributed to incorporation of P in excess of equilibrium partitioning during rapid growth, such that zoning patterns primarily record crystal growth rate variations (e.g., Toplis and Carroll, 1995; Milman-Barris et al., 2008; Shea et al., 2015; Baziotis et al., 2017a). Few other minerals have been examined for their P content or zoning patterns. In particular, there is minimal information in the literature about P-rich zones in pyroxenes — only six high-P pyroxenes ($P_2O_5 > 0.5$ wt%) can be found in the worldwide GEOROC compilation (Sarbas and Nohl, 2008) and there are limited experiments on its incorporation (Boesenberg and Hewins, 2010). Yet many of the processes that enrich olivine in P could also plausibly affect pyroxene, which can also grow rapidly in supersaturated melts and incorporate excess P due to its incompatibility and slow diffusion. No previous study has attempted to quantify the implications of the presence, concentration, or zoning of P in clinopyroxene.

In this study we consider the potential of P in clinopyroxene as a petrogenetic indicator and geospeedometer, based on two contrasting occurrences of high-P pyroxene in mantle xenoliths. First, we report the results of detailed micro-scale petrological and geochemical analyses on the constituent minerals and glass in one previously undescribed sample (*Ci-1-105a*) from the H. G. Wilshire collection of xenoliths from the Cima Volcanic Field (CVF - California, USA) and one recently collected xenolith (MA-1) from Morocco (Middle Atlas Mountains, Bou Ibalghatene). We used a range of complementary instruments — optical microscope, electron probe microanalyzer (EPMA) and laser-ablation Inductively Coupled Mass Spectrometry (LA-ICP-MS) — to characterize the texture and chemistry of the Moroccan host lava, the xenolith matrix minerals, and the various phases (glass and crystalline) in the melt pocket and veins. Spatially resolved analyses show that the exotic second-generation P-rich clinopyroxene grains found in glassy regions of the Cima Volcanic Field xenolith are homogeneous, whereas the Moroccan pyroxene is zoned in P. To interpret these observations, we first examine whether the P concentrations are anomalous given the overall budget of P in the melt pocket and veins and then consider the implications for incorporation mechanisms of P in pyroxene, for growth rates, and for timescales of melt infiltration events in the lithosphere. We illustrate

that our two cases span a considerable range of timescales and suggest that investigation of similar occurrences in other settings will constrain their timescales of formation as well.

GEOLOGICAL SETTING AND SAMPLE DESCRIPTION

Geological Setting

Cima Volcanic Field

The Cima Volcanic Field is located in the Mojave Desert, southeastern California, USA. The Cima Volcanic Field experienced activity from ~7.5 Ma to ~3 Ma, a hiatus, and then reactivation from ~1 Ma into the Holocene (Turrin et al., 1985; Nealey and Sheridan, 1989; Wells et al., 1991). It is one of many small and isolated late Cenozoic basaltic fields distributed across the southern Basin and Range province. Regional crustal extension of the Basin and Range (since about 12 Ma; Davis et al., 1993) has been accommodated in the crust by major range-bounding normal faults and Cordilleran metamorphic core complexes with synchronous felsic volcanism and in the mantle by lithospheric thinning associated with subsequent mafic volcanism. The Cima Volcanic Field is an alkaline basalt-dominated field, containing only trachybasalt (hawaiite) and basaltic trachyandesite (Wilshire et al., 1988, 1991; Mukasa and Wilshire, 1997). For more details on the Cima Volcanic Field and geological context for the broader area of the Mojave Desert, refer to Luffi et al. (2009) and Baziotis et al. (2017a).

Middle Atlas

The Moroccan xenolith is from a maar located in the Middle Atlas Mountains, Bou Ibalghatene area (31°9'48''N, 5°03'36''W). The volcanism in the area follows the NE trend of the North Middle Atlas fault and has been associated with thinning of the continental lithosphere by transtensional tectonics. The volcanoes in the area are each monogenetic, single eruptions of alkaline lava (nephelinites, basanites or alkali basalts; El Azzuzi et al., 1999, 2010). For more details about the maar, refer to Raffone et al. (2009) and El Messbahi et al. (2014).

Sample Description - Mantle Xenoliths

Cima Volcanic Field xenolith suite

The Cima Volcanic Field has yielded a rich variety of xenoliths (Irving, 1980; Farmer et al., 1995), divided by Wilshire et al. (1991) and Wilshire and McGuire (1996) into

three main groups: 1) “Cr-diopside” group (peridotite, websterite, phlogopite \pm pargasite clinopyroxenite), 2) “low-Cr green-pyroxene” group (Mg-rich websterite, two-pyroxene gabbro, microgabbro) and 3) “Al-augite” group (Fe-rich websterite, clinopyroxenite, gabbro and microgabbro). There is also a fourth group, composite xenoliths composed of two or more of the previous lithologies or containing hornblendite \pm plagioclase \pm phlogopite veins up to 15 mm in width. Sample *Ci-1-105a* from the Howard Wilshire collection archived at the Smithsonian Institution (NMNH 118016-118) is such a composite xenolith. It is amphibole-bearing, with clear alternating lherzolite and clinopyroxenite layers. It was selected for study on the basis of promise as a sample of preserved boundaries between mantle lithologies that partially melted in contact (Baziotis et al., 2017a). The host lava of the Cima xenolith is not preserved in our hand-specimen, but is presumed to be the typical trachybasalt of the Cima Volcanic Field.

Moroccan Xenoliths

Several of the Middle Atlas maar outcrops contain ultramafic xenoliths with a variety of lithologies, including a full spectrum of fertility from harzburgites through spinel lherzolites and wehrlites to pyroxenites. Several mantle xenoliths, including *MA-1*, were collected during a field trip to the Middle Atlas organized in conjunction with the 6th Orogenic Lherzolite Conference in Marrakech in 2014. The criteria for the selection of the studied xenoliths were freshness and integrity of specimens and the presence of melt veins. The specimen described here, labeled *MA-1*, is a porphyroclastic spinel-bearing lherzolite with scarce amphibole (Mercier and Nicolas, 1975); the host lava is preserved in a section prepared from a different xenolith, collected <10 m away, in the same flow.

ANALYTICAL METHODS

Scanning Electron Microscope (SEM)

We examined sample *Ci-1-105a* on the California Institute of Technology (Caltech) GPS Zeiss 1550VP field-emission scanning electron microscope, equipped with an angle-sensitive backscattered electron detector and a 150 mm² active area Oxford X-Max Si-drift-detector energy-dispersive X-ray spectrometer (EDS). Imaging, mapping, and semi-quantitative EDS analysis were conducted using the SmartSEM and AZtec software packages. Analyses used a 15 kV accelerating potential and a 120 μ m field aperture in high-current mode (\sim 4 nA probe current), yielding imaging resolution

better than 3 nm and an activation volume for EDS analysis $\sim 1 \mu\text{m}^3$. Maps are presented in qualitative mode, showing uncorrected intensity of the relevant X-ray counts at each pixel.

Major elements

Major element compositions of minerals were determined in polished thin sections using three electron microprobes. Both the JEOL JXA8900 Superprobe at the Agricultural University of Athens (Greece) and the CAMECA SX-100 at the University of Vienna Department of Lithospheric Research (Austria) are equipped with four wavelength-dispersive spectrometers (WDS) and one EDS. The JEOL JXA8530F field emission microprobe at the Institut für Mineralogie, University of Münster (Germany) has an additional WDS. All analyses were performed with an accelerating voltage of 15 kV. For minerals, a 20 nA focused beam current, 20 s counting time on peak position and 10 s for each background were used. Phosphorus concentrations in olivines and clinopyroxenes were then re-analyzed at 50 nA beam current with 20 s peak and 10 s background counting time. The detection limit for P with this protocol is 71 ppm (1σ). For glass analyses, a slightly defocused (5 μm diameter) beam and 10 s counting time were used. Natural mineral standards used were albite (Na, Si, Al), wollastonite (Ca), olivine (Mg), almandine (Fe), spessartine (Mn), orthoclase (K), rutile (Ti), chromite (Cr), Ni-oxide (Ni) and Durango apatite (P). Representative mineral compositions are given in Tables 1-3, while all data are given in the supplementary table S1. We see no evidence of interlaboratory bias between the three electron microprobes but we have not done a specific round-robin of replicate analyses to verify this. In any case, the conclusions of this study would not be affected by systematic differences between the three microprobes at the percent level.

Trace elements

Trace element abundance analyses were carried out at University of Münster on a Thermo Fisher Scientific Element 2 magnetic-sector ICP-MS coupled to a Photon Machines Analyte G2 Excimer laser system operating with ca. 5 J/cm² laser fluence and a repetition rate of 6-10 Hz. We used a large-volume ablation cell with fast signal response and short wash-out times (< 1 s) that holds up to six conventional thin sections and additional reference materials. Prior to sample analyses, the system was tuned with NIST SRM 612 glass for high sensitivity, stability, and low oxide-interference rates ($^{232}\text{Th}^{16}\text{O}/^{232}\text{Th} < 0.2\%$). Spot sizes for the mineral analysis were

between 12 and 60 μm in diameter; in most cases 40 μm was selected as the best compromise between laser signal strength and spatial resolution. The signal ablation time was 40 seconds for the peak and 20 seconds for the background. Wash out time between individual spots was 10 seconds. NIST SRM 612 glass (Jochum et al., 2011) was used as an external standard and the BIR-1G glass (Jochum et al., 2005) as an unknown to monitor precision and accuracy; Si, Mg and Ca served as internal standards for olivine/orthopyroxene, spinel and clinopyroxene/amphibole, respectively. Five to ten sample measurements were always bracketed by three measurements of NIST SRM 612 glass and two measurements of BIR-1G glass. Representative trace element analyses are given in Table 4-6, while all data are given in Table S2. Finally, data for the two standard glasses (individual measurements, means, standard deviation, relative standard deviation, and detection limits) are given in Table S2.

PETROGRAPHY

Matrix

Ci-1-105a

Sample *Ci-1-105a* is a multi-layered mantle xenolith containing alternating layers of porphyroclastic olivine clinopyroxenite and coarse-grained lherzolite (Fig. S1). The studied section is dominantly lherzolite, with a gradational and somewhat irregular transition to clinopyroxenite. The orthopyroxene modal abundance in lherzolite is low enough that some areas could be classified as wehrlite. The overall mineral assemblage includes olivine, clinopyroxene, orthopyroxene, spinel, amphibole and phlogopite. Small (<100 μm), interstitial, allotriomorphic spinel grains are widespread along grain boundaries. In several places, amphibole is rimmed by dark brown glass suggesting partial melting, perhaps upon decompression. A distinct dark-coloured zone, described in more detail below, contains melt veins that coalesce or accumulate to form melt pockets (Fig. 1). There is no evident geometrical relation between host fabrics and the vein population. The studied region is from an interior cut of the xenolith and is not in contact with the host lava.

MA-1

Sample *MA-1* is a medium- to coarse-grained porphyroclastic spinel lherzolite in contact with the host alkali basalt. The lherzolite is foliated and contains melt veins

that are both parallel and oblique to the foliation. Olivine is the predominant mineral phase (58 vol.%), forming subhedral to anhedral grains (1-2.4 mm) with widespread strain features such as undulose extinction, kink bands and sub-grains (Fig. S2). Olivine neoblasts (400-1000 μm in diameter) with polygonal grain boundaries occur along olivine and orthopyroxene boundaries. Orthopyroxene (29 vol. %) grain sizes are bimodal, with porphyroclasts (> 3 mm in diameter) and smaller, elongated grains (0.5-2 mm in diameter). Both types are sub- to anhedral with well-developed single cleavage planes and clinopyroxene exsolution lamellae (Fig. S2,2). Clinopyroxene (11 vol. %) with weak pale green pleochroism is found as interstitial, anhedral grains (0.5-1.4 mm) (Fig. S2,2). Spinel (2 vol.%) is found as elongated interstitial grains (0.3-1.6 mm) and as spongy corroded rims over spinel associated with glassy areas (Fig. 2b). Scarce, anhedral relics of brown pleochroic amphibole and bundles of platy phlogopite associated with spongy spinel are also present (Fig. 2a), surrounded by fine-grained aggregates of olivine + clinopyroxene + spinel \pm glass.

Host basalt of MA-1

The host basalt displays a characteristic vitrophyric texture. The matrix is dominated by glass, phenocrystic clinopyroxene and olivine. Idiomorphic clinopyroxene phenocrysts usually display a characteristic sieve texture. Orthopyroxene xenocrysts are rimmed by coronas of clinopyroxene and olivine xenocrysts are characterized by skeletal rims, both indicating reaction of the xenocrysts with the lava host. Numerous olivine crystallites, along with minor plagioclase and spinel, are also scattered in glass. Scarce amygdules filled with calcite are present.

“Dark-coloured” areas

Ci-1-105a

An irregularly-shaped (average ~ 2 mm wide) dark-coloured melt pocket is present between matrix olivine and clinopyroxene (Fig. 1). The melt pocket consists of olivine + glass (5-10 vol %) + plagioclase + spinel + clinopyroxene + apatite and is interpreted as a rapidly crystallized melt, suggested by the presence of glass and quench textures. In contact with glass, olivine shows an outer high-backscatter (Fe-rich) rim, typically 5-10 μm wide. Plagioclase occurs as prismatic, un-oriented crystals associated with clinopyroxene. Spinel occurs as inclusions in the olivine or in association with plagioclase and glass, showing euhedral to anhedral shape.

Clinopyroxene enclosed by melt within the pocket is euhedral to anhedral; larger euhedral grains have a high-backscatter rim 5-10 μm wide. Apatite occurs both as a large crystal (up to $\sim 100 \mu\text{m}$) near the rim of the pocket and as tiny dispersed crystals.

MA-1

Glass is found in several distinct features in *MA-1*: both in pockets around amphibole and in dark-coloured veins about $\sim 100 \mu\text{m}$ wide on average. Some of these veins are parallel to layering, whereas another set clearly crosscuts the foliation (Fig. 2).

Amphibole melt pocket: A melt pocket up to 1 mm across contains pleochroic brown amphibole relics (up to $250 \mu\text{m}$ wide) and is surrounded by secondary olivine + clinopyroxene + spinel + glass (Fig. 2). The entire pocket is included within a primary olivine grain in the lherzolite matrix. Amphibole is subhedral, with homogenous cores and backscatter-bright rims; epitaxial growth of secondary cpx is common around the amphibole rims. Olivine is present as scattered subhedral crystals ($20\text{-}80 \mu\text{m}$) within the pocket, with abundant spinel inclusions and backscatter-bright rims. Clinopyroxene ($10\text{-}90 \mu\text{m}$) with spinel inclusions forms subhedral crystals either within the pocket or epitaxially grown on amphibole. Complex core-rim and hourglass zoning are commonly observed. Spinel, besides being a chadacryst in secondary olivine and clinopyroxene, is also present as small euhedral to subhedral crystals in the glass.

Parallel Melt Veins: The parallel melt veins are generally composed of olivine + clinopyroxene + plagioclase + spinel + phlogopite + glass and are usually well crystallized with minor interstitial glass, generally below 10 vol. % (Fig. 2). Iron-rich rims of the matrix olivines in contact with the parallel melt veins suggest reaction between matrix and vein. Olivine grains inside the parallel melt veins include both phenocrysts (usually idiomorphic with spinel and rare, rounded glassy inclusions) and xenocrysts (zoned, with skeletal rims suggesting disequilibrium). Clinopyroxene is abundant, both euhedral grains and spindly quench crystals. Occasionally, the larger clinopyroxene crystals display compositional zoning. Clinopyroxene also grows from matrix orthopyroxene along the boundaries of the parallel melt veins. Plagioclase occurs as prismatic, flow-oriented crystals parallel or sub-parallel to the melt vein elongation. Spinel is usually found as anhedral to subhedral grains with characteristic

zonation towards Fe-rich rims. Phlogopite is quite rare and is found only along the boundary of the parallel melt veins, in close association with spinel and olivine.

Cross-cutting melt veins: Cross-cutting melt vein #1 is up to 200 μm wide in places (the widest vein in the studied specimen), and is oblique ($\sim 45^\circ$) to the foliation. It is mainly composed of olivine + clinopyroxene + spinel + apatite + glass. The abundance of glass in this vein reaches up to 15 vol. % (i.e., higher than in the parallel melt veins). Olivine is usually present as euhedral crystals that often contain spinel or ilmenite inclusions. In rare cases, rounded glass inclusions in olivine were identified. Rare fragments of matrix olivine (xenocrysts) display skeletal, Fe-rich rims, much like in-place matrix olivine along the boundary of the melt veins. Clinopyroxene is present again both as euhedral and as quenched, dendritic crystals $\leq 10 \mu\text{m}$ wide. In addition, clinopyroxene forms rims on matrix orthopyroxene grains that contact the glass of the melt vein. Spinel, when not included in other phases, is found as both anhedral and euhedral grains associated with olivine and glass. Spinel in contact with glass is zoned, with spongy, Fe-rich rims. Apatite is found rarely as small ($\leq 15 \mu\text{m}$ wide) subhedral crystals embedded in glass.

Cross-cutting melt veins #2 and #3 are two members of a separate set of melt veins oriented almost perpendicular to the foliation of the xenolith. The width of the glass-bearing portion of these veins rarely exceeds 100 μm , though they are bounded by additional rims of secondary cpx up to 10 μm wide wherever the veins cut through or abut matrix orthopyroxene. The veins are mainly composed of olivine + clinopyroxene + spinel + plagioclase + glass. Secondary olivine is present as euhedral to subhedral crystals, locally abundant in the marginal parts of the veins, and as high-backscatter overgrowths on matrix olivine. Secondary olivine may contain rounded spinel and glass inclusions. Clinopyroxene forms anhedral dendritic crystals with distinct high-backscatter rims; their grain sizes decrease towards the center lines of the veins. Plagioclase is present as lath-shaped crystals, occupying the central part of the veins and as an interstitial phase. Interstitial glass forms about 15 vol. % of the veins and is intimately mixed with randomly-oriented plagioclase laths.

MINERAL CHEMISTRY

The major and trace element compositions of minerals within melt-related areas (veins and pockets) are presented in this section. Due to the small size of several grains, some of the mineral phases were difficult or impossible to analyze. Here we emphasize those results that indisputably correspond to single grain analyses and identify mixed analyses when necessary.

Olivine

In *Ci-1-105a*, the melt pocket contains homogeneous olivines (Fo_{88.5}) with P₂O₅ ~ 0.08 wt%, richer in P than the matrix olivines (P₂O₅ in the range 0.02-0.06 wt% and Fo₈₄₋₈₉). The Li concentrations vary from 4.03 to 5.49 ppm; B content is remarkably constant (1.39-1.56 ppm). Vanadium and Sc display variation within a fairly restricted range compared to the other studied samples, from 2.26 to 7.36 ppm and from 2.07 to 6.30 ppm, respectively. The olivines have Ni content in the range 2140-2250 ppm and low to moderate (27-150 ppm) Cr abundances. The total REE concentrations range from 0.140 to 0.86 ppm.

Olivine in the amphibole melt pocket is magnesian (Fo₉₁₋₉₄) with normal zoning. Up to 0.08 wt% P₂O₅ is present, with highest concentrations adjacent to the rims. Concentrations of NiO and Cr₂O₃ are variable, 0.18-0.37 wt% and 0.07-0.23 wt%, respectively. Due to the small size of secondary olivine in the amphibole melt pocket, no clean LA-ICP-MS spot could be obtained and the electron probe analyses may be contaminated, so these analyses will not be discussed further.

Olivine in the parallel melt veins displays normal (Fo₈₆₋₉₂) zoning (scarce homogenous Fo₉₁ crystals are also present), mostly low P₂O₅ concentration (up to 0.07 wt%), and variable NiO (0.24-0.45 wt%) and Cr₂O₃ (0.01-0.20 wt%) contents. The Li concentrations vary from 2.08 to 3.58 ppm; B content spans from 0.88-6.65 ppm. Vanadium (up to 2.76 ppm) and Sc (up to 3.49 ppm) are relatively enriched compared to the other studied samples. The total REE concentrations are variable, from 1.27 to 4.86 ppm. There is also a distinctive population of strongly zoned, anhedral olivine grains with core compositions matching the matrix olivine (Fo₈₈₋₉₀, NiO 0.27-0.35 wt%, Cr₂O₃ 0.01-0.04 wt%) surrounded by outer rims (Fo₈₂₋₈₃) with up

to 0.26 wt% P_2O_5 . These are interpreted as matrix xenocrysts entrapped in the infiltrating melt, with reaction or overgrowth processes forming the rims.

A large, euhedral olivine in cross-cutting melt vein #1 displays a homogenous (Fo_{83}) core, overgrown by a less forsteritic rim (Fo_{81}). The rim is enriched in P_2O_5 (up to 0.17 wt%), in contrast with the homogenous core domain (0.04-0.07 wt% P_2O_5). NiO (0.10-0.19 wt%) and Cr_2O_3 (0.01-0.04 wt%) are low and relatively homogenous. The core displays low concentrations of Li (~1.45 ppm), V (~1 ppm), Sc (1.21 ppm), and total REE (1.183 ppm).

In cross-cutting melt vein #2, olivine displays a wide range in forsterite component, normally zoned from Fo_{91} to Fo_{82} ; Fo is correlated with large variations in NiO (0.41-0.07 wt%) and Cr_2O_3 (0.02-0.13 wt%) contents. There are large variations in P_2O_5 concentration, 0.003-0.78 wt%, but domains with $P_2O_5 > 0.1$ wt% are only found in more evolved zones (Fo_{82-85}), whether in phenocrysts or at the outer rims of anhedral xenocrysts.

Clinopyroxene

In the melt pocket in *Ci-1-105a*, clinopyroxene is Al- and Ti-rich but projects into the Wo-En-Fs ternary at $Wo_{44-50}En_{36-46}Fs_{10-17}$ (notably more Fe-rich than other clinopyroxene analyses; see Fig. 3a). The concentration of P_2O_5 (by EPMA) in the various clinopyroxene grains examined ranges from 0.11 to 0.68 wt%, but mapping shows that each grain is homogeneous in P_2O_5 content. The primitive-mantle normalized trace element patterns are similar to those observed at the rims of matrix clinopyroxene adjacent to the melt pocket; they are characterized by negative Ba, Pb, Sr-P, Zr-Hf, and Li anomalies and relatively flat patterns from Th to Pr (Fig. 4a). The chondrite-normalized rare earth element (REE) patterns are concave-down from light to middle REE and essentially flat in the heavy REE (Fig. 4c).

In *MA-1*, clinopyroxene in the amphibole melt pocket projects to $Wo_{42-46}En_{46-54}Fs_{4-10}$ (Fig. 3b) and is variable in TiO_2 (0.15-2.45 wt%), Al_2O_3 (4.42-10.17 wt%) and Cr_2O_3 (0.08-2.44 wt%) contents, with increasing Al_2O_3 and TiO_2 towards the rim (Table 2). The concentration of P_2O_5 is relatively low (0.01-0.15 wt%). The normalized trace element patterns in the clinopyroxene core are depleted in large-ion lithophile elements (LILE) with negative Ba, Pb, Sr-P, Zr-Hf, Ti and V anomalies, but positive

Li anomalies. Patterns are relatively flat from Gd to Lu (Fig. 5a). The patterns near the rims are similar except for distinctive enrichment in LILE. Secondary clinopyroxene cores in the amphibole melt pocket display a distinctive (Fig. 5) REE pattern: concave downwards in the LREE ($\text{La}/\text{Sm}_N = 1.06\text{-}1.18$), slight negative Eu anomaly ($0.87\text{-}0.93$), gently descending MREE to HREE ($\text{Dy}/\text{Yb}_N = 1.24\text{-}1.29$), and high total REE concentrations (815-870 ppm). On the other hand, the rims are more enriched in LREE ($\text{La}/\text{Sm}_N = 2.59\text{-}4.60$), may lack a Eu anomaly ($0.91\text{-}1.01$), show more fractionated MREE to HREE ($\text{Dy}/\text{Yb}_N = 1.72\text{-}1.92$), and overall have more variable total REE content (720-920 ppm).

In parallel melt veins, clinopyroxene is notably less calcic ($\text{Wo}_{36\text{-}42}\text{En}_{51\text{-}57}\text{Fs}_{5\text{-}8}$), with variable Al_2O_3 (2.46-8.58 wt%) and Cr_2O_3 (0.12-2.59 wt%) concentrations and notably lower TiO_2 (0.22-1.15 wt%) than other secondary clinopyroxenes in the sample. The concentration of P_2O_5 is low, ≤ 0.08 wt%. The PM-normalized trace element patterns show positive Ba, Pr, Nd, Sm, and Li anomalies alongside negative Pb, Zr-Hf, Ti, and V anomalies and flat patterns from Gd-Yb. Rare earth element patterns have a monotonic negative slope from LREE to HREE ($\text{La}/\text{Yb}_N = 6.51$) with a small negative Eu anomaly ($\text{Eu}/\text{Eu}^* = 0.77$) and elevated total REE concentration (1590 ppm).

Clinopyroxene in cross-cutting melt vein #1 show substantial variation in FeO and MgO contents ($\text{Wo}_{43\text{-}46}\text{En}_{37\text{-}51}\text{Fs}_{4\text{-}19}$), with normal core-rim zoning. Large variations are observed in TiO_2 (0.20-7.19 wt%), Al_2O_3 (4.17-9.61 wt%) and Cr_2O_3 (up to 0.69 wt%) contents (Table 2). There is a large range of P_2O_5 concentrations (0.03-1.18 wt%), positively correlated with Al_2O_3 and TiO_2 and showing maximum values adjacent to crystal rims. Trace element patterns are more enriched in LILE than in clinopyroxene from parallel melt veins, with negative Ta, Pb, Zr-Hf anomalies, positive Nb and La anomalies, and smoothly descending patterns from Nd to Sc. The REE pattern displays strongly fractionated LREE/HREE ($\text{La}/\text{Yb}_N = 15.8$), less fractionated MREE/HREE, and high REE concentrations (REE = 4950 ppm).

In cross-cutting melt vein #2, secondary clinopyroxene ($\text{Wo}_{38\text{-}43}\text{En}_{50\text{-}57}\text{Fs}_{5\text{-}10}$) displays more restricted ranges in FeO, MgO, TiO_2 (0.14-2.12 wt%) and Al_2O_3 (2.01-7.58 wt%) alongside higher and more variable Cr_2O_3 (0.05-1.78 wt%), compared to cross-

cutting melt vein #1. The content of P_2O_5 is negligible, with maximum values ~ 0.06 wt%.

Plagioclase

In *Ci-1-105a*, plagioclase composition covers the range $An_{53-64}Ab_{33-42}Or_{3-5}$. In *MA-1*, plagioclase in cross-cutting melt vein #2 is variable in composition, $An_{29-57}Ab_{40-64}Or_{2-7}$, whereas plagioclase in parallel melt veins is restricted to the calcic end of this range ($An_{44-57}Ab_{42-53}Or_{1-5}$).

Glass

In the melt pocket in *Ci-1-105a*, EPMA analyses on glass reveal a K_2O -rich composition (7.01-7.86 wt%) with P_2O_5 content up to 1.23 wt%. Unfortunately, the glass areas between quench crystals are too small to obtain LA-ICP-MS analyses uncontaminated by adjacent phases, so the trace element budget in the glass is not known from this sample.

In *MA-1*, glasses in amphibole melt pocket are silica-undersaturated (Fig. 6), with low to intermediate SiO_2 (48.1-55.9 wt%), moderate to high Na_2O (5.81-9.00 wt%), and moderate to high K_2O content (2.84-6.50 wt%). The range in P_2O_5 concentration is 0.58-1.25 wt%. There is a positive correlation between MgO (0.85-2.41 wt%) and CaO (1.59-6.68 wt%), but these oxides are negatively correlated with Al_2O_3 (17.7-20.4 wt%), total FeO (3.50-7.48 wt%), and TiO_2 (1.48-2.18 wt%) (Fig. 7). Trace element patterns are concave-up across the LILE, with positive anomalies in Rb, Nb-Ta, and Li alongside negative anomalies in Pb, Ti and Sc (Fig. 5). The REE pattern shows a descending slope from LREE to HREE ($La/Yb_N=17.80$), slight negative Eu anomaly ($Eu/Eu^*=0.86$) and total REE concentration of 1110 ppm (Fig. 5).

Glasses in parallel melt veins are also silica-undersaturated (Fig. 6), with low to moderate SiO_2 (45.7-55.8 wt%), moderate to high Na_2O (4.50-8.06 wt%), and variable K_2O (0.69-5.75 wt%). The concentration of P_2O_5 extends up to 1.05 wt%. The contents of CaO (4.69-9.44 wt%), FeO (3.68-6.28 wt%), and TiO_2 (0.49-2.21 wt%) decrease with decreasing MgO (0.85-3.14 wt%), whereas Al_2O_3 (17.9-21.7 wt%) and K_2O increase (Fig. 7). Trace element patterns show positive anomalies in Rb, Nb-Ta, and Li alongside negative anomalies in Pb, Ti and Sc (Fig. 5b). The REE

pattern is significantly fractionated LREE to HREE ($\text{La/Yb}_N=28.9$), lacks any Eu anomaly, and has high total REE concentration, 10300 ppm (Fig. 5d).

Compared to glass in the parallel melt veins, analyzed glass in cross-cutting melt vein #1 has higher SiO_2 content (46.1-49.3 wt%), more variable Na_2O content (1.23-8.15 wt%), and systematically lower K_2O (1.65-3.17 wt%) (Fig. 6). The concentration of P_2O_5 is relatively high, ranging from 0.89-2.31 wt%. Plotted against the limited range of MgO (0.94-3.11 wt%), Al_2O_3 increases (16.3-19.6 wt%) as MgO decreases, whereas FeO (6.96-11.5 wt%), CaO (4.55-10.7 wt%) and TiO_2 (2.03-3.50 wt%) all decrease (Fig. 7). Concentrations of Na_2O are too scattered to discern any trend. Trace element patterns are characterized by depleted LILE and positive anomalies in Th, Rb, Nb-Ta, and Li alongside negative anomalies in U, Pb, Ti and Sc (Fig. 5b). The REE pattern is even more fractionated overall than observed in the parallel melt veins ($\text{La/Yb}_N=30.9$), with no Eu anomaly and high total REE concentrations, 6570 ppm (Fig. 5d).

Glass in cross-cutting melt vein #2, analyzed by electron microprobe only, is more evolved than glass from cross-cutting melt vein #1, with 50.2-58.6 wt% SiO_2 (Fig. 6). There is a negative correlation between SiO_2 and MgO (1.04-3.64 wt%) but a positive correlation between SiO_2 and Al_2O_3 . Contents of Na_2O (0.33-7.41 wt%) are variable; K_2O concentration (1.62-5.54 wt%) is somewhat less variable. Positive correlations are observed among MgO , CaO , FeO , and TiO_2 (Fig. 7). Concentrations of P_2O_5 vary across an order of magnitude (0.09-1.18 wt%).

Apatite

Three apatite grains were analyzed for trace elements in *Ci-1-105a*. The trace-element patterns are characteristic of the strongly fractionating crystal chemistry of apatite, with negative Nb, Zr and V-Sc anomalies relative to the primitive mantle and high Th and U abundances in the range of $1000\times$ PM (Fig. 4). The REE yield extremely strong LREE enrichment [$(\text{La/Yb})_N=95-127$], slight negative Eu anomalies ($\text{Eu}/\text{Eu}^*=0.75-0.80$), moderately fractionated MREE [$(\text{Gd/Yb})_N=4.88-5.06$] and total REE concentrations in the range of 2960-3060 ppm (Fig. 4).

Spinel

In the melt pocket in *Ci-1-105a*, secondary spinel is uniform in composition with molar $Al\# = Al/(Al+Fe^{3+}+Cr) = 0.82$ and $Cr\# = Cr/(Cr+Al) = 0.14$. In *MA-1*, spinel in the amphibole melt pocket displays an intermediate Mg-spinel-chromite composition with $Al\# = 0.55-0.56$ and $Cr\# 0.40-0.41$. In parallel melt veins, spinel composition approaches the Mg-rich end-member, with high $Al\# = 0.65-0.80$ and variable $Cr\# = 0.16-0.31$. Secondary spinel in cross-cutting melt vein #1 is Ti-rich, displaying an intermediate magnetite-ulvöspinel composition with homogenous $Al\# = 0.24-0.26$ and more variable $Cr\# = 0.03-0.17$.

DISCUSSION

Phosphorus partitioning in clinopyroxene

Perhaps the most exceptional observation in both xenoliths is the presence of P-rich clinopyroxene. X-ray maps of with a high-resolution field-emission scanning electron microscope reveal no evidence, at the highest achievable magnification, of hotspots or P-rich inclusion phases. The P appears to be incorporated in the pyroxene structure itself (Figs. 9,10c).

We found 509 xenolith-hosted clinopyroxene analyses in the GEOROC database (Sarbas and Nohl, 2008); 81.7% (415 analyses) have <0.1 wt% P_2O_5 ; 49 analyses have 0.1-0.2 wt% P_2O_5 , 40 analyses have 0.2-0.3 wt% P_2O_5 , and the maximum P_2O_5 is 0.66 wt%. In the Cima Volcanic Field case, we find clinopyroxene grains with unzoned P_2O_5 contents up to 0.68 wt%. In the Moroccan case, clinopyroxene in one of the studied cross-cutting melt veins has P_2O_5 content reaching ~ 1.2 wt% at the rim. Note that glass adjacent to the clinopyroxene rims has ≤ 2.31 wt% P_2O_5 , insufficient to generate the measured P counts in the pyroxene, tens of μm from the glass, by secondary fluorescence artifacts (Brunet and Chazot, 2001).

Reports of elevated P in pyroxene are exceedingly scarce. GEOROC (Sarbas and Nohl, 2008) includes only six other occurrences with $P_2O_5 > 0.5$ wt.% worldwide. These reports include convergent margin and intraplate tectonic settings, in nephelinite, basanite, and pyroxenite (e.g., Yurtmen, 2000; Solovova et al., 2005; Liu et al., 2010a,b). The P-rich pyroxenes in *Ci-1-105a* are close to the compositions reported in the groundmass of basanite (Yurtmen et al., 2000), with similar SiO_2 and Al_2O_3 , and slightly higher TiO_2 contents. All the P-rich pyroxene analyses in *MA-1* with ≥ 1.0 wt% P_2O_5 , however, have lower SiO_2 , higher Al_2O_3 , and higher TiO_2

contents than previously reported high-P pyroxene. On the other hand, analysis points in MA-1 with ≤ 1.0 wt% P_2O_5 overlap the compositions of moderately P-bearing pyroxene from the database.

As P-rich clinopyroxene is so rare, there has been little discussion of its origin and significance, in contrast to the extensive studies of P-rich olivine (e.g., Toplis et al., 1994; Milman-Barris et al., 2008; Mallmann et al., 2009; Boesenberg and Hewins, 2010; Grant and Kohn, 2013; Shearer et al., 2013; Welsch et al., 2014; McCanta et al., 2016; Baziotis et al., 2017a; Gordeychik et al., 2018). Here we consider how insights gained from the interpretation of P in olivine might apply to clinopyroxene.

Substitution mechanism

Dendritic pyroxene found in a natural iron-carbon alloy from Disko Island (Greenland) contains up to 2.6 wt% P_2O_5 (more commonly in the range 1-2 wt%; Goodrich, 1984). Extremely P-rich pyroxene (up to 30 wt% P_2O_5) was produced experimentally by Boesenberg and Hewins (2010), who suggested that the complexity of the substitution mechanism for P in the pyroxene structure may be the major reason that so few natural P-rich pyroxenes have been found. The substitution mechanisms are thought to involve P^{+5} on tetrahedral sites, compensated by some mix of trivalent ions and vacancies on tetrahedral sites or by coupled substitutions on octahedral sites (e.g., Boesenberg and Hewins, 2010).

The P contents of clinopyroxene in this study are plotted in Figure 8 versus Si atoms per formula unit (apfu) (Fig. 8a,c) and Ti/Al ratio (Fig. 8b,d). In *Ci-1-105a*, there is initially negative correlation between Si cations and P (correlation coefficient $r = -0.50$), giving way to constant Si (~ 1.6 apfu) in the upper range of P contents. This suggests that P readily substitutes for Si up to a certain concentration, beyond which other coupled substitutions are required. On the other hand, in *MA-1*, P and Si apfu are negatively correlated ($r = -0.76$) over the whole range of P concentrations (Fig. 8b). The P-rich pyroxene, when recast into a 10-component stoichiometry (Excel spreadsheet written by Michael Marks and modified by Paul Asimow), contains mostly $\leq 3\%$ of the Ca-Tschermak ($CaAlAlSiO_6$) component, because most of the Al^{3+} compensates for Ti substitution, shown by a 8-24% Ti-Tschermak ($CaTiAl_2O_6$) component (Table 2). Phosphorus content is positively correlated with Ti/Al ($r = 0.63$ for *MA-1* and $r = 0.74$ for *Ci-1-105a*), but only up to ~ 0.25 wt% P_2O_5 , after which

Ti/Al reaches a constant value (Fig. 8b,d). In the extremely reducing Disko Island setting, Goodrich (1984) showed that P-rich pyroxenes with high Ti/Al ratios might be associated with the presence of Ti^{3+} but the Cima Volcanic Field shows no evidence (such as phosphides, Fe-Cr alloys, etc.) for such reducing conditions (Fig. 8b). There is some increase in Na apfu with increasing P in *Ci-1-105a* ($r = 0.79$), suggesting a $NaMgPSiO_6$ component, however the *MA-1* data show no such relationship ($r = -0.15$). In general, the substitution mechanism in clinopyroxene in the melt pocket in *Ci-1-105a* at the highest P end of the correlation is obscure, whereas in cross-cutting melt vein #1 in *MA-1*, substitution for Si with various charge-balancing mechanisms is viable over the full range of observed concentrations.

X-ray maps of P-rich clinopyroxene from melt pockets in *Ci-1-105a* show no zonation of P content (Fig. 9). This is somewhat surprising, as phenocrystic pyroxenes are commonly zoned, even in rapidly diffusing components such as Mg# and Mn, as well as the slowly diffusing cations Ca, Cr, Ti, and Al (e.g., Cherniak and Dimanov, 2010; Cherniak and Liang, 2012). We collected detailed EPMA line traverses across one clinopyroxene from the *Ci-1-105a* melt pocket, which show slight zonation in Mg, Ca and Al (Fig. 9i). Absent experimental work on the development or relaxation of P-zoning in pyroxene, we suggest that relaxation of either oscillatory or monotonic growth zoning in P is unlikely. The uniform enrichment observed therefore requires crystallization slow enough to avoid boundary enrichment and growth from a melt of constant P content. The constant P condition could result either from crystal growth in a large enough reservoir of uniform melt to avoid progressive P enrichment or growth of pyroxene after P concentration in the melt became buffered by apatite saturation. A large uniform reservoir is unlikely in an apparently isolated melt pocket and is inconsistent with the observed zoning in Li from adjacent, secondary olivines in the same melt pocket. Lithium does not encounter a buffering phase to limit its enrichment in residual liquid as crystallization proceeds. Hence, we favor apatite buffering to explain homogeneous P in clinopyroxene.

X-ray maps of a P-rich pyroxene in cross-cutting melt vein #1 in *MA-1* confirm the inference from spot analyses that P content is zoned, becoming enriched toward the rim (Fig. 10). This resembles the normal zonation seen in both rapidly (Fe, Mg) and slowly (Al, Ti, Cr, Ca) diffusing components in fast-growing crystals (Cherniak and Liang, 2012; Elardo and Shearer, 2014). The P enrichment toward the

rim might be explained by crystallization rapid enough to develop a P-rich boundary layer in front of the crystal facets as they advance into the melt; however, it might also reflect equilibrium growth of pyroxene in a restricted melt pool prior to melt saturation in apatite. These cases can be distinguished if equilibrium partition coefficients are known or estimated, by comparison to the apparent partition coefficient between the crystal rims and the quenched glass.

Proposed models for pyroxene growth

The mechanism of rapid crystal growth and formation of a boundary layer enriched in slowly-diffusing incompatible elements has been well-studied for olivine. Here we examine whether it can be extended to model zoned and unzoned clinopyroxene.

The diffusive snowplow model (Watson and Müller, 2009) predicts that the degree of disequilibrium in a trace element (i) is a function of its partition coefficient ($K_{d,i} \equiv \frac{C_i^{solid(eq)}}{C_i^{melt}}$, where eq indicates equilibrium concentration), its diffusivity in the melt (D_i), the crystal growth rate (G), and the thickness of the boundary layer (BL). If dynamical stirring maintains a fixed-width boundary layer, the steady state concentration of an element that arises at finite growth rate, $C_i^{solid(diseq)}$, is given by:

$$C_i^{solid(diseq)} = \frac{C_i^{solid(eq)}}{1 - (1 - K_{d,i})\frac{G}{D_i}BL}. \quad (1)$$

For a given crystal that grew at a certain rate surrounded by a certain boundary layer, G and BL would be the same for all elements. This suggests that the degree of disequilibrium ($Q_i \equiv 1 - \frac{C_i^{solid(eq)}}{C_i^{solid(diseq)}}$, which is 0 at equilibrium and tends to 1 for large excess concentrations and towards $-\infty$ for concentrations much less than equilibrium) for various elements in a crystal should scale as $SP_i = (1 - K_{d,i})/D_i$. Specifically, we expect $Q_i = G \cdot BL \cdot SP_i$. Note that Q_i should be positive for incompatible elements and negative for compatible elements.

Zoning developed during crystal growth may be later modified by diffusive relaxation. Watson et al. (2015) inferred an upper limit of a months at magmatic temperature for preservation of $\sim 5 \mu\text{m}$ wide P-rich bands in olivine. We will not explicitly model post-growth storage of clinopyroxene at magmatic temperatures here, but its effect is only to relax original gradients and so our estimated growth rates will

be minima: storage between formation of the glass vein and eruption would imply more rapid growth during the formation of the vein.

Consider the observed concentrations of every analyzed trace element in clinopyroxene rims and adjacent glass in xenolith MA-1 from Morocco. Given an estimate of the equilibrium $K_{d,i}$ for each element, the glass analysis allows us to estimate $C_i^{solid}(eq) = K_{d,i}C_i^{melt}$ and then, with the analysis of the crystal rim, to calculate Q_i . We compiled a set of partition coefficients appropriate for clinopyroxene in alkali basalt (Table 7) and another set appropriate for clinopyroxene in basaltic andesite (Table 7); these should provide reasonable estimates of the equilibrium partition coefficients likely to apply to the melt veins in our xenoliths. Next, we compiled estimates of diffusivity D_i of each trace element in the melt at 1250 °C (Li, Ti, and Pb from Zhang et al., 2010; P from Watson et al. 2015; other elements from Holycross and Watson, 2016; for Tm we averaged the coefficients of adjacent elements Er and Yb). We can then calculate the snowplow parameter $(1-K_{d,i})/D_i$ for each element for clinopyroxene growing into alkali basalt or basaltic andesite melt.

The results of this exercise (Figure 11) show, first, remarkably clear positive correlation between Q_i and $(1-K_{d,i})/D_i$ for both cross-cutting melt vein #1 and amphibole melt pocket cases, whichever set of partition coefficients are used. This implies that the dynamically stirred diffusive snowplow model is helpful for analysing the disequilibrium growth of the pyroxenes in these two settings. On the other hand, the parallel melt vein case is scattered. In fact, in the parallel melt veins the clinopyroxene is low in P_2O_5 (≤ 0.08 wt%) and shows no evidence of rapid crystal growth (crystal shapes are equant) or boundary enrichment, so failure to fit the snowplow model should be expected. The absence of simple positive correlation for parallel melt veins demonstrates that the correlation in the other cases is significant and not a tautological byproduct of having $K_{d,i}$ in both ordinate and abscissa). Second, for both cross-cutting melt vein #1 and amphibole melt pocket, the data can be reasonably well-fit with straight lines. Their slopes, according to equation (1), imply the following values of $G \cdot BL$ (in m^2/s , with uncertainties from the linear regression): $1.7 \pm 0.5 \times 10^{-12}$ (cross-cutting melt vein, basaltic andesite model), $3.5 \pm 0.6 \times 10^{-12}$ (cross-cutting melt vein, alkali basalt model), $4.5 \pm 0.7 \times 10^{-12}$ (amphibole melt pocket, basaltic andesite model) and $5.3 \pm 0.7 \times 10^{-12}$ (amphibole melt pocket, alkali basalt model). For a BL of order 100 μm (Watson and Müller, 2009), the implied

growth rates (in m/s) for the same four cases are $1.7 \pm 0.4 \times 10^{-8}$, $3.6 \pm 0.6 \times 10^{-8}$, $4.5 \pm 0.7 \times 10^{-8}$, and $5.3 \pm 0.7 \times 10^{-8}$, respectively. For typical zoned clinopyroxene grains with 50 μm long axes, we then estimate crystal growth times (in seconds) for the same four cases as 3000 ± 800 , 1400 ± 200 , 1100 ± 150 , and 900 ± 100 . MELTS calculations show that clinopyroxene grows within a ~ 100 $^{\circ}\text{C}$ segment of the liquid line of descent, such that these growth time estimates correspond to a cooling rate during that interval of ~ 0.1 $^{\circ}\text{C}/\text{s}$ (i.e., $\sim 10^2$ $^{\circ}\text{C}/\text{hr}$). Smaller estimates of BL correspond to faster growth rates and shorter growth times.

Petrogenetic history of the glassy regions

Our data suggest subtly different petrogenetic histories for the two xenoliths. Sample *Ci-1-105a* from the Cima Volcanic Field experienced the following stages: C1) melt intrusion and aggregation into pockets, C2) rapid initial cooling to near-equilibrium with the host, accompanied by olivine crystallization and reaction with matrix minerals, C3) slower crystallization in the sequence $\text{Ol} \rightarrow \text{Ap} \rightarrow \text{Cpx} \rightarrow \text{Pl} \rightarrow \text{Fe-Ox}$ and C4) quench of glass. On the other hand, *MA-1* from Morocco shows evidence of: M1) melt intrusion, M2) amphibole melting, M3) reaction with matrix minerals, M4) rapid crystallization of minerals through the sequence $\text{Ol} \rightarrow \text{Cpx} \rightarrow \text{Pl} \rightarrow \text{Ap} \rightarrow \text{Fe-Ox}$ and M5) quench of glass. Stages M3 and M4 may have been simultaneous and coupled by energy conservation constraints (Baziotis et al., 2017a). The quench may have affected different parts of the melt pocket or melt veins at different times and temperatures, helping to explain the diversity of observed glass compositions.

Stage M1, melt intrusion in *MA-1*, is indicated by the planar shape of some glassy regions and by the cross-cutting relation between glassy veins and the matrix fabric. Neither of these textural arguments applies to *Ci-1-105a*. However, both samples show evidence of reaction between the melt and matrix minerals, suggesting that the melts parental to the glasses were exotic to both host xenoliths rather than locally generated by partial melting. The co-existence of parallel and cross-cutting melt veins may indicate more than one generation of melt intrusion in *MA-1*.

Amphibole melting, stage M2, is indicated by corroded rims in contact with melt (now glass) that crystallized secondary olivine, pyroxene and Fe-Ti oxides. The amphibole melting may have accompanied decompression during entrainment and eruption in the host lava (in which case it could be temporally and causally unrelated

to the melt veins), or it may have been triggered by intrusion of the exogenous melt at stage M1.

Rapid cooling (stages C2 and M4) is suggested by the observed zoning in olivine (Baziotis et al., 2017a) and clinopyroxene. Slowly-diffusing P and rapidly-diffusing Li distributions yield upper and lower limits on the growth rate of secondary crystals. Early-crystallizing olivine grew rapidly enough to cause boundary layer enrichment of sluggish P but not so fast as to over-enrich other elements. This has been observed in P-rich olivines in melt veins from other Cima Volcanic Field xenoliths (Baziotis et al., 2017a) and in olivines from Moroccan xenoliths. The clinopyroxene in the melt pocket in *Ci-1-105a*, both neoblasts and reaction rims, formed after olivine, under slow enough growth conditions that P remained homogeneous (Fig. 9i,j). However, the preservation of Li zoning in olivine (Baziotis et al., 2017a), given the high diffusivity of Li (Qian et al., 2010), shows both that clinopyroxene growth cannot have been slow and that a limited amount of time passed between clinopyroxene growth and quench of the system. In the case of the Moroccan xenolith, at least the later stages of clinopyroxene growth were rapid enough to cause a diffusive boundary layer pileup effect and excess P incorporation near the pyroxene rim; the pyroxene cores may have grown more slowly (Fig. 10).

The different placement of the onset of apatite crystallization in the two studied cases is motivated both by the chemical argument about P zoning and by textural criteria. The absence of apatite inclusions in olivine rims places the onset of apatite crystallization after the bulk of olivine growth in both xenoliths. In *MA-1*, plagioclase shows evidence of flow alignment along the long direction of the melt veins, whereas apatite lacks a shape-preferred orientation, suggesting apatite growth at a later stage than plagioclase. In contrast, in *Ci-1-105a*, plagioclase and apatite in the melt pocket are both randomly oriented. The minor negative Eu anomalies ($\text{Eu}/\text{Eu}^* = 0.75\text{--}0.80$) observed in large apatites in *Ci-1-105a* may be inherited from the parental melt, but they may also indicate some early plagioclase fractionation preceding apatite growth.

Evolution of glass compositions

The simplest interpretation of the presence of variable glass compositions with the melt pocket in *Ci-1-105a* and within individual melt veins in *MA-1* is that different zones quenched to glass at different times during the evolution of the melt pocket or

veins. There are other plausible causes, including spatial inhomogeneity of simultaneously quenched melt compositions, variable alteration after quench, multiple generations of intrusion, etc. However, here we test the simple assumption that the glass samples progressive magmatic evolution in each pocket or vein. In this case, it is appropriate to compare the suite of glass analyses to models of processes such as simple fractional crystallization and assimilation coupled to fractional crystallization. We used the alphaMELTS interface to the MELTS model (<http://magmasource.caltech.edu>) to track both major and trace elements (Ghiorso and Sack, 1995; Asimow and Ghiorso, 1998; Asimow, 1999; Ghiorso et al., 2002; Asimow et al., 2001, 2004; Smith and Asimow, 2005). In this approach, one most often tests magmatic evolution from the most primitive (highest MgO) analysis, assessing whether its liquid line of descent passes through the more evolved compositions. We did not attempt to model the melt pocket in *Ci-1-105a* on the basis of only four, possibly contaminated, glass analyses. Instead we focus on the glass-bearing regions of Moroccan xenolith *MA-1*.

The one primitive analysis point with 6.0 wt% MgO was tested first, but it appears to be impossible for all the glasses to have a common parentage (Figs. S3,S4). Throughout a considerable parameter space of pressure, oxygen fugacity, and water content, none of the liquid lines of descent for fractional crystallization provide a satisfactory fit to any of the glass groups. The differences are well outside the range of analytical error: fitting CaO would require displacing the onset of clinopyroxene fractionation by about 2 wt% MgO, whereas fitting TiO₂ would require suppressing Fe-Ti oxide fractionation by 2.5 wt% MgO. The inability of fractional crystallization to fit the data is clear in a SiO₂ vs. Na₂O+K₂O plot (Fig. S3). Because the starting glass is alkalic (a foidite), its liquid line of descent experiences rapid alkali enrichment unlike the trends in the data. We are forced to reject the notion that the entire glass population can be modeled as a fractional crystallization trend. Given the petrographic evidence of reaction with matrix minerals, this conclusion is not surprising.

We next considered, fractional crystallization beginning at different compositions for each subgroup of glass analyses (parallel melt veins, cross-cutting melt veins) to see whether any of these subgroups lie on their own fractional crystallization trends. Alkalis in the cross-cutting melt vein glasses are uncorrelated with SiO₂ (Fig. 6), a behavior that does not arise in fractional crystallization models, so we abandoned this model for the cross-cutting melt vein glasses. On the other

hand, the parallel melt vein population shows more promise as a fractional crystallization trend. We selected the most primitive analysis in a parallel melt vein ($\text{MgO} = 3.14 \text{ wt\%}$) and examined its liquid line of descent in 1°C steps over a wide range of pressure (1 to 8 kb kbar), $f\text{O}_2$ (QFM -1 to $+1$) and H_2O content in the starting liquid (0.1 to 2.0 wt%). The conditions that best-fit the suite of parallel melt vein glasses were 5 kbar, QFM, and 2 wt% H_2O (Fig. 7). This model fits the inflections in the FeO_t and Al_2O_3 trends against MgO . It is plausible, therefore, that the parallel melt veins were injected as liquid and underwent effectively closed-system fractional crystallization at the identified conditions, quenching to glass at different temperatures and degrees of evolution and thereby preserving the differentiation history of the vein.

Glass analyses from the three different cross-cutting melt veins studied do not appear to be petrogenetically related. However, the numerous analyses of glass in cross-cutting melt vein #1 do show well-defined correlations of most elements versus MgO content [Correlation coefficients r for the oxides against MgO are: TiO_2 0.56, FeO_t 0.28, CaO 0.68, Al_2O_3 -0.75 , K_2O -0.64 , and P_2O_5 -0.40] usually a prerequisite for recognizing any simple petrogenetic evolution. However, Na_2O contents are scattered (r for MgO - Na_2O regression is -0.37), from low values $<1\%$ to extremely high values $>8\%$. No single model will be able to relate these compositions to one another unless there were good reason to neglect Na_2O . Although there is good correlation among other elements, MELTS modeling shows that the trend is not parallel to the fractional crystallization trend in SiO_2 vs. MgO or in TiO_2 vs. MgO . We examined a number of assimilation-fractional crystallization scenarios involving the matrix minerals (olivine, orthopyroxene or both) found along the melt vein boundaries. Despite examining isothermal models, isobaric cooling models, and isenthalpic models, we found no scenario that satisfactorily matches the major element correlations in cross-cutting melt vein #1. Together with the scattered Na_2O , we are left with the conclusion that disequilibrium processes were likely involved, and that an equilibrium code like MELTS is unable to extract the meaning of the compositional variation among the glass analyses from cross-cutting melt vein #1.

Incompatible element zonation and crystal shape as complementary kinetic tools

Rates of crystal growth and hence of cooling of melts to form igneous rocks are often inferred from crystal morphology, both crystal size distributions (Cashman and Ferry, 1988; Marsh, 1988; Higgins, 2000; Morgan and Jerram, 2006) and crystal shapes,

particularly plagioclase (Cabane et al., 2005; Pupier et al., 2008) and olivine (Helz, 1987; Faure et al., 2003; Welsch et al., 2013, 2014; Shea et al., 2015). A few studies have examined the shapes of pyroxene crystals in nature (Baziotis et al., 2017b) or experimentally quantified the rates needed to obtain hopper, dendritic, and spinifex morphologies (cooling rates $>10^{-7}$ cm/s, Kouchi et al., 1983; Mollo et al., 2010). Recent experiments by Welsch et al. (2016) suggest that clinopyroxene growth rate is extraordinarily sensitive to degree of undercooling, increasing by three orders of magnitude to values approaching 10^{-6} m/s between 45 °C and 55 °C below the liquidus. In the two xenolith cases studied, both secondary olivine and pyroxene display well-developed, non-dendritic crystal faces. On the basis of morphology alone, the interpretation is ambiguous: the shapes reflect a final stage of growth slower than that necessary to form complex shapes but they cannot rule out an earlier rapid dendritic phase that later filled in (Welsch et al., 2014).

Elemental concentrations and distributions in minerals offer another set of tools, with sensitivity to different timescales compared to morphological indicators. Olivine in particular has been widely used in recent years as a tracer of cooling rates, defining lower and upper limits in the range of a few to several °C/h. Enrichment of P in olivine above concentrations expected for equilibrium partitioning with coexisting glass suggests growth fast enough to develop a diffusive boundary layer in the melt adjacent to the moving crystal interface (e.g., Milman-Barris et al., 2008; Watson et al., 2015; Baziotis et al., 2017a). By contrast, preservation of such zoning for rapidly diffusing elements offers complementary bounds on storage times after crystal growth (Watson et al., 2015). Finely structured oscillatory zones of P enrichment often preserve evidence of rapid initial growth phases even when the outer shapes of the crystals show evidence only of a slower final growth phase.

Pyroxene is the second most abundant silicate mineral group in the Earth's upper mantle and is also abundant in mafic to intermediate igneous rocks, including many that are olivine-free. If pyroxene records rate-dependent information in concentration and zoning profiles of P, then it is important to dedicate instrument time to high-precision analyses of this element and to calibrate the interpretation of such analyses. However, the experimental data on equilibrium partitioning are scarcely adequate to characterize the range of behavior, given the complexity of pyroxene crystal chemistry and the wide range of melt compositions in which pyroxenes occur.

Although the two cases reported in this work are only the 7th and 8th localities in the world known to have high-phosphorus pyroxenes, we think it likely that the situation is analogous to that of P-rich olivine a decade ago. Phosphorus in clinopyroxene has not received much attention from scientists and it requires high current and long counting times to quantify precisely. Enhanced P content may be restricted to zones only ~1 μm wide and so may require mapping at high spatial resolution. A sound general approach to searching for and then quantifying the presence of minor elements calls for a hierarchical approach of survey measurements followed by re-analysis of interesting grains and zones. The precise determination of, e.g., P zoning at 1 μm scale by EPMA requires beam current of at least 50 nA and counting times more than 20-30 s for the peak. This time-consuming protocol is nevertheless effective and practical and offers phosphorus detection limits lower than 100 ppm (e.g., 71 ppm for the olivine analyses in Baziotis et al., 2017a).

CONCLUSIONS

Analysis of glass and secondary minerals in glass-bearing regions of mantle xenoliths of the Cima Volcanic Field and the Atlas Mountains revealed two varieties of exotic, phosphorus-rich clinopyroxene. Considering these crystals in the context of growth processes and kinetic phenomena leads to a number of inferences and conclusions about cooling rates and vein-host reactions. The xenolith glasses are the product of rapidly crystallized melt, accompanied in some cases by assimilation of host minerals. The unzoned P-rich clinopyroxene ($\text{P}_2\text{O}_5 \sim 0.6 \text{ wt}\%$) in a glassy pocket in a Cima Volcanic Field xenolith implies slow enough crystallization to avoid boundary enrichment and growth of clinopyroxene after P and volatile concentrations in the melt (perhaps only within the boundary layer around the growing crystals) became buffered by apatite saturation. In contrast, one cross-cutting glassy vein in the Moroccan xenolith hosts pyroxene with zoning in P_2O_5 extending up to 1.2 wt% at the outer rim. We attribute this to an accelerating rate of crystal growth, with onset of a diffusive boundary layer pileup effect and excess P incorporation near the pyroxene rim. These examples offer a preview of the potential application of P distribution in clinopyroxene as a geospeedometer in igneous rocks.

ACKNOWLEDGEMENTS

We thank the constructive comments raised by Dr. Anne Peslier, Dr. Emily J. Chin and an anonymous reviewer. Also, we are grateful to the associate editor Dr. James Day for his editorial handling and fruitful review. I.B. obtained funds for this research from the Action «Supporting Postdoctoral Researchers» of the Operational Program "Education and Lifelong Learning" of the General Secretariat for Research and Technology, co-financed by the European Social Fund (ESF) and the Greek State. I.B. and S.K. acknowledge the IKYDA academic exchange program between the Greek State Foundation and the Deutscher Akademischer Austauschdienst – DAAD. PDA is supported by the US NSF through award GI-1550934. I.B. would like to thank Theo Ntaflos for support with the electron probe microanalyses. This paper is dedicated to Larry Augustus Taylor, with deep respect from all the authors for his many long-lasting contributions to the study of terrestrial, lunar, and martian rocks. I.B. wishes to express what a great honor and inspiration it was to work with Larry as a postdoc and to have learned meteoritics and mantle xenolith studies from such a distinguished scientist.

REFERENCES

- Adam J. and Green T. (2006). Trace element partitioning between mica-and amphibole-bearing garnet lherzolite and hydrous basanitic melt: 1. Experimental results and the investigation of controls on partitioning behaviour. *Contributions to Mineralogy and Petrology* **152**(1), 1-17.
- Agrell S. O., Charnley N. R. and Chinner G. A. (1998). Phosphoran olivine from Pine Canyon, Piute Co., Utah. *Mineralogical Magazine* **62**, 265–269.
- Asimow P. D. (1999). A model that reconciles major-and trace-element data from abyssal peridotites. *Earth and Planetary Science Letters* **169**(3), 303-319.
- Asimow P. D. and Ghiorso M. S. (1998). Algorithmic modifications extending MELTS to calculate subsolidus phase relations. *American Mineralogist* **83**, 1127-1132.
- Asimow P. D., Hirschmann M. M. and Stolper E. M. (2001). Calculation of peridotite partial melting from thermodynamic models of minerals and melts, IV. Adiabatic decompression and the composition and mean properties of mid-ocean ridge basalts. *Journal of Petrology* **42**(5), 963-998.

- Asimow P. D., Dixon J. E. and Langmuir C. H. (2004). A hydrous melting and fractionation model for mid-ocean ridge basalts: Application to the Mid-Atlantic Ridge near the Azores. *Geochemistry, Geophysics, Geosystems* **5**(1).
- Baker M. B. and Wyllie P. J. (1992). High-pressure apatite solubility in carbonate-rich liquids: implications for mantle metasomatism. *Geochimica et Cosmochimica Acta* **56**(9), 3409-3422.
- Baziotis I., Asimow P. D., Ntaflos T., Boyce J. W., McCubbin F. M., Koroneos A., ... and Klemme S. (2017a). Phosphorus zoning as a recorder of crystal growth kinetics: application to second-generation olivine in mantle xenoliths from the Cima Volcanic Field. *Contributions to Mineralogy and Petrology* **172**(7), 58.
- Baziotis, I., Economou-Eliopoulos, M. and Asimow, P. D. (2017b). Ultramafic lavas and high-Mg basaltic dykes from the Othris ophiolite complex, Greece. *Lithos* **288**, 231-247.
- Beattie, P. (1993). The generation of uranium series disequilibria by partial melting of spinel peridotite: constraints from partitioning studies. *Earth and Planetary Science Letters* **117**(3-4), 379-391.
- Boesenberg J.S. and Hewins R.H. (2010). An experimental investigation into the metastable formation of phosphoran olivine and pyroxene. *Geochimica et Cosmochimica Acta* **74**, 1923-1941
- Boesenberg J. S., Delaney J. S. and Hewins R. H. (2012). A petrological and chemical reexamination of Main Group pallasites formation. *Geochimica et Cosmochimica Acta* **89**, 134-158.
- Brunet F. and Chazot G. (2001). Partitioning of phosphorus between olivine, clinopyroxene and silicate glass in a spinel lherzolite xenolith from Yemen. *Chemical Geology* **176**(1), 51-72.
- Cabane H., Laporte D. and Provost A. (2005). An experimental study of Ostwald ripening of olivine and plagioclase in silicate melts: implications for the growth and size of crystals in magmas. *Contributions to Mineralogy and Petrology* **150**(1), 37-53.
- Cashman, K. V. and Ferry, J. M. (1988). Crystal size distribution (CSD) in rocks and the kinetics and dynamics of crystallization. *Contributions to Mineralogy and Petrology* **99**(4), 401-415.
- Cherniak D. J. and Dimanov A. (2010). Diffusion in pyroxene, mica and amphibole. *Reviews in Mineralogy and Geochemistry* **72**(1), 641-690.

- Cherniak D. J. and Liang Y. (2012). Ti diffusion in natural pyroxene. *Geochimica et Cosmochimica Acta* **98**, 31-47.
- Davis G. A., Fowler T. K., Bishop K., Brudos T. C., Friedmann S. J., Parke M. L. and Burchfiel B.C. (1993). Pluton pinning of an active Miocene detachment fault system eastern Mojave Desert, California. *Geology* **21**, 267-270.
- Demouchy S., Jacobsen S. D., Gaillard F. and Stern C. R. (2006). Rapid magma ascent recorded by water diffusion profiles in mantle olivine. *Geology* **34**(6), 429-432.
- Demouchy S., Ishikawa A., Tommasi A., Alard O. and Keshav S. (2015). Characterization of hydration in the mantle lithosphere: Peridotite xenoliths from the Ontong Java Plateau as an example. *Lithos* **212-215**, 189-201.
- Dostal J., Dupuy C., Carron J. P., De Kerneizon M. L. G. and Maury R. C. (1983). Partition coefficients of trace elements: application to volcanic rocks of St. Vincent, West Indies. *Geochimica et Cosmochimica Acta* **47**(3), 525-533.
- Elardo S. M. and Shearer C. K. (2014). Magma chamber dynamics recorded by oscillatory zoning in pyroxene and olivine phenocrysts in basaltic lunar meteorite Northwest Africa 032. *American Mineralogist* **99**, 355-368.
- Ennis M. E. and McSween H. Y. (2014). Crystallization kinetics of olivine-phyric shergottites. *Meteoritics and Planetary Science* **49**(8), 1440-1455.
- Ewart A., Bryan W. B. and Gill J. B. (1973). Mineralogy and geochemistry of the younger volcanic islands of Tonga, SW Pacific. *Journal of Petrology* **14**(3), 429-465.
- Farmer G. L., Glazner A. F., Wilshire H. G., Wooden J. L., Pickthorn W. J. and Katz M. (1995). Origin of late Cenozoic basalts at the Cima volcanic field, Mojave Desert, California. *Journal of Geophysical Research* **100**, 8399-8415.
- Faure, F., Trolliard, G., Nicollet, C. and Montel, J. M. (2003). A developmental model of olivine morphology as a function of the cooling rate and the degree of undercooling. *Contributions to Mineralogy and Petrology* **145**(2), 251-263.
- Foley S. F., Prelevic D., Rehfeldt T. and Jacob D. E. (2013). Minor and trace elements in olivines as probes into early igneous and mantle melting processes. *Earth and Planetary Science Letters* **363**, 181-191.
- Forsythe L. M., Nielsen R. L. and Fisk M. R. (1994). High-field-strength element partitioning between pyroxene and basaltic to dacitic magmas. *Chemical Geology* **117**(1-4), 107-125.

- Fujimaki H., Tatsumoto M. and Aoki K. I. (1984). Partition coefficients of Hf, Zr, and REE between phenocrysts and groundmasses. *Journal of Geophysical Research: Solid Earth* **89**(S02), B662-B672.
- Gallahan W. E. and Nielsen R. L. (1992). The partitioning of Sc, Y, and the rare earth elements between high-Ca pyroxene and natural mafic to intermediate lavas at 1 atmosphere. *Geochimica et Cosmochimica Acta* **56**(6), 2387-2404.
- Ghiorso M. S. and Sack R. O. (1995). Chemical mass transfer in magmatic processes IV. A revised and internally consistent thermodynamic model for the interpolation and extrapolation of liquid-solid equilibria in magmatic systems at elevated temperatures and pressures. *Contributions to Mineralogy and Petrology* **119**(2-3), 197-212.
- Ghiorso M. S., Hirschmann M. M., Reiners P. W. and Kress V. C. (2002). The pMELTS: A revision of MELTS for improved calculation of phase relations and major element partitioning related to partial melting of the mantle to 3 GPa. *Geochemistry, Geophysics, Geosystems* **3**(5), 1-35.
- Goodrich C. A. (1984). Phosphoran pyroxene and olivine in silicate inclusions in natural iron-carbon alloy, Disko Island, Greenland. *Geochimica et Cosmochimica Acta* **48**(5), 1115-1126.
- Gordeychik B., Churikova T., Kronz A., Sundermeyer C., Simakin A. and Wörner G. (2018). Growth of, and diffusion in, olivine in ultra-fast ascending basalt magmas from Shiveluch volcano. *Scientific reports* **8**(1), 11775.
- Grant T. B. and Kohn S. C. (2013). Phosphorus partitioning between olivine and melt: An experimental study in the system $\text{Mg}_2\text{SiO}_4\text{-Ca}_2\text{Al}_2\text{Si}_2\text{O}_9\text{-NaAlSi}_3\text{O}_8\text{-Mg}_3(\text{PO}_4)_2$. *American Mineralogist* **98**, 1860-1869.
- Hack P. J., Nielsen, R. L. and Johnston A. D. (1994). Experimentally determined rare-earth element and Y partitioning behavior between clinopyroxene and basaltic liquids at pressures up to 20 kbar. *Chemical Geology* **117**(1-4), 89-105.
- Hart S. E. and Brooks C. (1974). Clinopyroxene-matrix partitioning of K, Rb, Cs, Sr and Ba. *Geochimica et Cosmochimica Acta* **38**(12), 1799-1806.
- Hart S. R. and Dunn T. (1993). Experimental cpx/melt partitioning of 24 trace elements. *Contributions to Mineralogy and Petrology* **113**(1), 1-8.
- Hauri E. H., Wagner T. P. and Grove T. L. (1994). Experimental and natural partitioning of Th, U, Pb and other trace elements between garnet, clinopyroxene and basaltic melts. *Chemical Geology* **117**(1-4), 149-166.

- Helz, R. T. (1987). Diverse olivine types in lava of the 1959 eruption of Kilauea volcano and their bearing on eruption dynamics. *US Geological Survey Professional Paper* **1350**(1), 691-722.
- Higgins, M. D. (2000). Measurement of crystal size distributions. *American Mineralogist* **85**(9), 1105-1116.
- Hilchie L., Fedortchouk Y., Matveev S. and Kopylova M. G. (2014). The origin of high hydrogen content in kimberlitic olivine: Evidence from hydroxyl zonation in olivine from kimberlites and mantle xenoliths. *Lithos* **202**, 429-441.
- Holycross M. E., and Watson E. B. (2016). Diffusive fractionation of trace elements in basaltic melt. *Contributions to Mineralogy and Petrology* **171**(10), 80.
- Irving A. J. (1980). Petrology and geochemistry of composite ultramafic xenoliths in alkali basalts and implications for magmatic processes within the mantle. *American Journal of Science* **280-A**, 389-426.
- Irving A. J. and Frey F. A. (1984). Trace element abundances in megacrysts and their host basalts: constraints on partition coefficients and megacryst genesis. *Geochimica et Cosmochimica Acta* **48**(6), 1201-1221.
- Jenner G. A., Foley S. F., Jackson S. E., Green T. H., Fryer B. J. and Longerich H. P. (1993). Determination of partition coefficients for trace elements in high pressure-temperature experimental run products by laser ablation microprobe-inductively coupled plasma-mass spectrometry (LAM-ICP-MS). *Geochimica et Cosmochimica Acta* **57**(23-24), 5099-5103.
- Jochum K. P., Willbold M., Raczek I., Stoll B. and Herwig K. (2005). Chemical Characterisation of the USGS Reference Glasses GSA-1G, GSC-1G, GSD-1G, GSE-1G, BCR-2G, BHVO-2G and BIR-1G Using EPMA, ID-TIMS, ID-ICP-MS and LA-ICP-MS. *Geostandards and Geoanalytical Research* **29**, 285–302.
- Jochum K. P., Weis U., Stoll B., Kuzmin D., Yang Q., Raczek I., Jacob D. E., Stracke A., Birbaum K., Frick D. A., Günther D. and Enzweiler J. (2011). Determination of Reference Values for NIST SRM 610–617 Glasses Following ISO Guidelines. *Geostandards and Geoanalytical Research* **35**, 397–429.
- Johnson K. T. M. (1994). Experimental cpx/and garnet/melt partitioning of REE and other trace elements at high pressures: petrogenetic implications. *Mineralogical Magazine A* **58**, 454-455.

- Johnson K. T. M. and Kinzler R. J. (1989). Partitioning of REE, Ti, Zr, Hf, and Nb between clinopyroxene and basaltic liquid: An ion microprobe study. *Eos Trans. AGU* **70**, 1388.
- Kouchi A., Sugawara Y., Kashima K. and Sunagawa I. (1983). Laboratory growth of sector zoned clinopyroxenes in the system $\text{CaMgSi}_2\text{O}_6$ - $\text{CaTiAl}_2\text{O}_6$. *Contributions to Mineralogy and Petrology* **83**(1-2), 177-184.
- Liu Y., Gao S., Hu Z., Gao C., Zong K. and Wang D. (2010a). Continental and oceanic crust recycling-induced melt-peridotite interactions in the trans-North China orogen: U-Pb dating, Hf isotopes and trace elements in zircons from mantle xenoliths. *Journal of Petrology* **51** (1-2), 537-571.
- Liu S., Su W., Hu R., Feng C., Gao S., Coulson I. M., Wang T., Feng G., Tao Y. and Xia Y. (2010b). Geochronological and geochemical constraints on the petrogenesis of alkaline ultramafic dykes from southwest Guizhou Province, SW China. *Lithos* **114**(1), 253-264.
- Luffi P., Saleeby J. B., Lee C.-T. A. and Ducea M. N. (2009). Lithospheric mantle duplex beneath the central Mojave Desert revealed by xenoliths from Dish Hill, California. *Journal of Geophysical Research* **114**, B03202, doi: 10.1029/2008JB005906.
- de Maisonneuve C. B., Costa F., Huber C., Vonlanthen P., Bachmann O. and Dungan M. A. (2016). How do olivines record magmatic events? Insights from major and trace element zoning. *Contributions to Mineralogy and Petrology* **171**(6), 56.
- Mallmann G., O'Neill H. C. St. and Klemme S. (2009). Heterogeneous distribution of phosphorus in olivine from otherwise well-equilibrated spinel peridotite xenoliths and its implications for the mantle geochemistry of lithium. *Contributions to Mineralogy and Petrology* **158**, 485-504.
- Marsh, B. D. (1988). Crystal size distribution (CSD) in rocks and the kinetics and dynamics of crystallization. *Contributions to Mineralogy and Petrology* **99**(3), 277-291.
- Matsui Y., Onuma N., Nagasawa H., Higuchi H. and Banno S. (1977). Crystal structure control in trace element partition between crystal and magma. *Tectonics* **100**, 315-324.
- McDonough W. F. and Sun S. S. (1995). The composition of the Earth. *Chemical geology* **120**(3-4), 223-253.

- Mercier J. C. and Nicolas A. (1975). Textures and fabrics of upper mantle peridotites as illustrated by xenoliths from basalts. *Journal of Petrology* **16**, 454–487.
- Milman-Barris M. S., Beckett J. R., Baker M. B., Hofmann A. E., Morgan Z., Crowley M. R., Vielzeuf D. and Stolper E. (2008). Zoning of phosphorus in igneous olivines. *Contributions to Mineralogy and Petrology* **155**, 739-765.
- Mollo S., Del Gaudio P., Ventura G., Iezzi G. and Scarlato P. (2010). Dependence of clinopyroxene composition on cooling rate in basaltic magmas: implications for thermobarometry. *Lithos* **118**(3-4), 302-312.
- Morgan, D. J. and Jerram D. A. (2006). On estimating crystal shape for crystal size distribution analysis. *Journal of Volcanology and Geothermal Research* **154**(1-2), 1-7.
- Mukasa S. B. and Wilshire H. G. (1997). Isotopic and trace element compositions of upper mantle and lower crustal xenoliths, Cima volcanic field, California: Implications for evolution of the subcontinental lithospheric mantle. *Journal of Geophysical Research* **102**, 20133-20148.
- Nealey L. D. and Sheridan M. F. (1989). Post-Laramide volcanic rocks of Arizona and northern Sonora, Mexico, and their inclusions. *Geologic evolution of Arizona: Arizona Geological Society Digest* **17**, 609-648.
- Nicholls I. A. and Harris K. L. (1980). Experimental rare earth element partition coefficients for garnet, clinopyroxene and amphibole coexisting with andesitic and basaltic liquids. *Geochimica et Cosmochimica Acta* **44**(2), 287-308.
- Peslier A. H., Woodland A. B. and Wolff J. A. (2008). Fast kimberlite ascent rates estimated from hydrogen diffusion profiles in xenolithic mantle olivines from southern Africa. *Geochimica et Cosmochimica Acta* **72**(11), 2711-2722.
- Peslier A. H. and Bizimis M. (2014). H diffusion in olivine and pyroxene from peridotite xenoliths and a Hawaiian magma speedometer. *Lunar and Planetary Science and Exploration, Goldschmidt*, 8-13 June, Sacramento, California.
- Pupier E., Duchene S. and Toplis M. J. (2008). Experimental quantification of plagioclase crystal size distribution during cooling of a basaltic liquid. *Contributions to Mineralogy and Petrology* **155**(5), 555-570.
- Qian Q., O'Neill H. S. C. and Hermann J. (2010). Comparative diffusion coefficients of major and trace elements in olivine at ~ 950° C from a xenocryst included in dioritic magma. *Geology* **38**(4), 331-334.

- Reid F. (1983). Origin of the rhyolitic rocks of the Taupo Volcanic Zone, New Zealand. *Journal of Volcanology and Geothermal Research* **15**(4), 315-338.
- Ronov A. B. and Yaroshevsky A. A. (1976). A new model of chemical composition of the Earth crust. *Geokhimiya* **12**, 1763.
- Sakya P. A., Tanaka R., Kobayashi K., and Nakamura E. (2012). Inherited Pb isotopic records in olivine antecryst-hosted melt inclusions from Hawaiian lavas. *Geochimica et Cosmochimica Acta* **95**, 169-195.
- Sarbas B. and Nohl U. (2008). The GEOROC database as part of a growing geoinformatics network. In: Brady SR, Sinha AK, Gundersen LC (eds.) Geoinformatics 2008—data to knowledge. In: Proceedings: U.S. geological survey scientific investigations report 2008–5172, pp 42/43.
- Schneider P., Tropper P. and Kaindl R. (2013). The formation of phosphoran olivine and stanfieldite from the pyrometamorphic breakdown of apatite in slags from a prehistoric ritual immolation site (Goldbichl, Igls, Tyrol, Austria). *Mineralogy and Petrology* **107**(2), 327-340.
- Schulte-Pelkum V., Biasi G., Sheehan A. and Jones C. (2011). Differential motion between upper crust and lithospheric mantle in the central Basin and Range. *Nature Geoscience* **4**(9), 619-623.
- Shea T., Lynn K. J. and Garcia M. O. (2015). Cracking the olivine zoning code: Distinguishing between crystal growth and diffusion. *Geology* **43**(10), 935-938.
- Shearer C. K., Aaron P. M., Burger P. V., Guan Y., Bell A. S. and Papike J. J. (2013). Petrogenetic linkages among fO_2 , isotopic enrichments-depletions and crystallization history in Martian basalts. Evidence from the distribution of phosphorus in olivine megacrysts. *Geochimica et Cosmochimica Acta* **120**, 17-38.
- Shimizu H. (1980). Experimental study on rare-earth element partitioning in minerals formed at 20 and 30kb for basaltic systems. *Geochemical Journal* **14**(4), 185-202.
- Skulski T., Minarik W. and Watson E. B. (1994). High-pressure experimental trace-element partitioning between clinopyroxene and basaltic melts. *Chemical Geology* **117**(1-4), 127-147.
- Smith P. M. and Asimow P. D. (2005). Adiatat_1ph: A new public front-end to the MELTS, pMELTS, and pHMELTS models. *Geochemistry, Geophysics, Geosystems* **6**(2).
- Solovova I. P., Giris A. V., Kogarko L. N. and Kononkova N. N. (2005). Compositions of magmas and carbonate-silicate liquid immiscibility in the Vulture alkaline igneous complex, Italy. *Lithos* **85**, 113-128.

- Spandler C., O'Neill H. S. C. and Kamenetsky V. S. (2007). Survival times of anomalous melt inclusions from element diffusion in olivine and chromite. *Nature* **447**(7142), 303-306.
- Sun S. S., and McDonough W. F. (1989). Chemical and isotopic systematics of oceanic basalts: implications for mantle composition and processes. Geological Society, London, Special Publications, **42**(1), 313-345.
- Toplis M. J., Libourel G. and Carroll M. R. (1994). The role of phosphorus in crystallisation processes of basalt: an experimental study. *Geochimica et Cosmochimica Acta* **58**(2), 797-810.
- Toplis M. J. and Carroll M.R. (1995). An experimental study of the influence of oxygen fugacity on Fe–Ti oxide stability, phase relations, and mineral–melt equilibria in ferro-basaltic systems. *Journal of Petrology* **36**, 1137–1170.
- Tschegg C., Ntaflos T., Kiraly F. and Harangi S. (2010). High temperature corrosion of olivine phenocrysts in pliocene basalts from Banat, Romania. *Austrian Journal of Earth Sciences* **103**(1), 101-110.
- Tropper P., Recheis A. and Konzett J. (2004). Pyrometamorphic formation of phosphorus-rich olivines in partially molten metapelitic gneisses from a prehistoric sacrificial burning site (Ötz Valley, Tyrol, Austria). *European journal of mineralogy* **16**(4), 631-640.
- Turrin B. D., Dohrenwend J. C., Drake R. E. and Curtis G. H. (1985). K-Ar ages from the Cima volcanic field, eastern Mojave Desert, California. *Isochron West* **44**, 9–16.
- Villemant B., Jaffrezic H., Joron J. L. and Treuil M. (1981). Distribution coefficients of major and trace elements; fractional crystallization in the alkali basalt series of Chaîne des Puys (Massif Central, France). *Geochimica et Cosmochimica Acta* **45**(11), 1997-2016.
- Warren J. M. and Hauri E. H. (2014). Pyroxenes as tracers of mantle water variations. *Journal of Geophysical Research: Solid Earth* **119**(3), 1851-1881.
- Watson E. B. and Müller T. (2009). Non-equilibrium isotopic and elemental fractionation during diffusion-controlled crystal growth under static and dynamic conditions. *Chemical Geology* **267**, 111–124.
- Watson E. B., Cherniak D. J. and Holycross M. E. (2015). Diffusion of phosphorus in olivine and molten basalt. *American Mineralogist* **100**, 2053-2065.

- Wells S. G., McFadden L. D. and Olinger C. T. (1991). Use of cosmogenic ^3He and ^{21}Ne to understand desert pavement formation (abstract). *Geological Society of America Abstracts* **23**, 206.
- Welsch B., Faure F., Famin V., Baronnet A. and Bachèlery P. (2013). Dendritic crystallization: A single process for all the textures of olivine in basalts?. *Journal of Petrology* **54**(3), 539-574.
- Welsch B., Hammer J. and Hellebrand E. (2014). Phosphorus zoning reveals dendritic architecture of olivine. *Geology* **42**, 867-870.
- Welsch B., Hammer J., Baronnet A., Jacob S., Hellebrand E. and Sinton J. (2016). Clinopyroxene in postshield Haleakala ankaramite: 2. Texture, compositional zoning and supersaturation in the magma. *Contributions to Mineralogy and Petrology* **171**(1), 6.
- Wilshire H. G., Meyer C. E., Nakata J. K., Calk L. C., Shervais J. W., Nielson J. E. and Schwarzman E. C. (1988). Mafic and ultramafic xenoliths from volcanic rocks of the western United States. United States Geological Survey Professional Paper 1443, 179 pp.
- Wilshire H. G., McGuire A. V., Noller J. S. and Turrin B. D. (1991). Petrology of lower crustal and upper mantle xenoliths from the Cima volcanic field, California. *Journal of Petrology* **32**, 169–200.
- Wilshire H. G. and McGuire A. V. (1996). Magmatic infiltration and melting in the lower crust and upper mantle beneath the Cima volcanic field, California. *Contributions to Mineralogy and Petrology* **123**, 358-374.
- Wood B. J. and Trigila R. (2001). Experimental determination of aluminous clinopyroxene–melt partition coefficients for potassic liquids, with application to the evolution of the Roman province potassic magmas. *Chemical Geology* **172**(3), 213-223.
- Yurtmen S., Rowbotham G., İşler F. and Floyd P. A. (2000). Petrogenesis of basalts from southern Turkey: the Plio-Quaternary volcanism to the north of Iskenderun Gulf. *Geological Society London Special Publications* **173**(1), 489-512.
- Zack T. and Brumm R. (1998). Ilmenite/liquid partition coefficients of 26 trace elements determined through ilmenite/clinopyroxene partitioning in garnet pyroxenites. In International Kimberlite Conference: Extended Abstracts (Vol. 7, No. 1, pp. 986-988).

Zhang Y., Ni H. and Chen Y. (2010). Diffusion data in silicate melts: *Reviews in Mineralogy and Geochemistry* **72**, 311–408.

ACCEPTED MANUSCRIPT

Figure Captions

Figure 1. Back-scattered electron images of Ci-1-105a. (a) Typical melt pocket surrounded by matrix olivine, clinopyroxene and orthopyroxene. Large apatite grains (white) have concave boundaries suggesting partial resorption. (b) Enlarged view emphasizing Fe-enrichment at rims (lighter grey colour in back-scattered electron image) of olivine and cpx. At left, two P-rich clinopyroxene (P-Cpx) grains are indicated. (c) Part of the crystallized assemblage of the melt pocket composed of plagioclase (Pl), P-rich clinopyroxene, spinel, glass and quench crystals. (d) High-magnification view of quench texture in melt pocket, emphasizing the difficulty of obtaining glass analyses uncontaminated by surrounding phases in this specimen. Abbreviations: Ol: olivine; Cpx: clinopyroxene; P-Cpx: phosphorus-rich clinopyroxene; Pl: plagioclase; Ap: apatite.

Figure 2. (a-c) Optical microscope images of matrix minerals from the MA-1 xenolith of Morocco. (d-f) Back-scattered electron images of (d) matrix and (e, f) melt vein minerals. Abbreviations: Ol: olivine; Cpx: clinopyroxene; Opx: orthopyroxene; Spl: spinel; Pl: plagioclase; Amp: amphibole; Phl: phlogopite; Gl: glass; Mp: melt pocket; Mv: melt vein.

Figure 3. Pyroxene compositional range projected into the Di-Hd-En-Fs ternary. Analyses range from augite to diopside while covering a significant range in Fe content (squares: Ci-1-105a; triangles: MA1).

Figure 4. Trace element patterns (a,b) and rare earth elements (c,d) for sample Ci-1-105a. The samples are normalized to primitive mantle (PM) for (a) clinopyroxene, and (b) apatite, and to CI chondrite meteorite for (c) clinopyroxene and (d) apatite. Abbreviations: Cpx: clinopyroxene; Ap: apatite. The normalisation values for primitive mantle (PM) from Sun and McDonough (1989) and for CI chondrite are from McDonough and Sun (1995).

Figure 5. Trace element patterns (a,b) and rare earth elements (c,d) for sample MA-1 and basalt from MA-2. The samples are normalized as in figure 4.

Figure 6. Total-alkali Silica (TAS) diagram including glasses from the melt veins, amphibole-bearing melt pocket and preserved basalt of sample MA-1. Abbreviations: CMV1: cross-cutting melt vein #1; CMV2: cross-cutting melt vein #2; AMP: amphibole melt pocket; PMV: parallel melt vein.

Figure 7. MgO (in wt%) variation diagrams for major oxides (in wt%) for glass analyses in sample MA-1. Abbreviations as in figure 6.

Figure 8. Scatter plots of individual EPMA analysis spots in clinopyroxene, comparing P^{5+} to (a,c) Si^{4+} and (b,d) Ti/Al for sample Ci-1-105a (a,b) and MA-1 (c,d). Furthermore, there are enough counts to get ~1% relative precision just from counting statistics except on all the points with ≥ 0.02 apfu P. However, the random errors are smaller than the sizes of the symbols thus we choose to eliminate them from the figures.

Figure 9. Qualitative X-ray maps (a-d) of P-rich clinopyroxenes, outlined in white, from sample Ci-1-105a. The numbers on the P maps indicate P_2O_5 wt% from EPMA spot analyses.

Figure 9. continued. High resolution BSE image (e) and qualitative X-ray maps (f-i) showing P-rich clinopyroxenes in melt pocket from Ci-1-105a. In (j, k) two rim-rim EPMA signal profiles on P-rich clinopyroxenes designated in (h). Both profiles suggest homogeneous P content in both crystals.

Figure 10. (a) P-rich clinopyroxene in melt (now glassy) vein associated with secondary olivine. (b) Compositional rim-rim profile of the clinopyroxene indicated in (a). (c) Qualitative X-ray maps of P-rich clinopyroxene for Al, Ti, Ca, Mg, Na and P. The P X-ray map suggests an extended low-P core, surrounded by high-P toward the rim.

Figure 11. Assessments of disequilibrium between clinopyroxene and glass using the suite of analyzed trace elements for the MA-1 xenolith of Morocco. Predicted concentrations in clinopyroxene computed from coexisting glass analyses and published partition coefficients relative to measured clinopyroxenes are plotted using a snowplow model for melt composition of alkali-basalt (a) and basaltic-andesite (b). The two adopted sets of partition coefficients of clinopyroxene/melt are listed in Table 7. The snowplow parameter (SP_{-i}) is defined as $(1-K_{d,i})/D_i$, where $K_{d,i}$ is the partition coefficient ($K_{d,i} \equiv \frac{c_i^{solid}(eq)}{c_i^{melt}}$; i : refers to a particular trace element and (eq) indicates an equilibrium concentration) and D_i corresponds to the diffusivity in the melt.

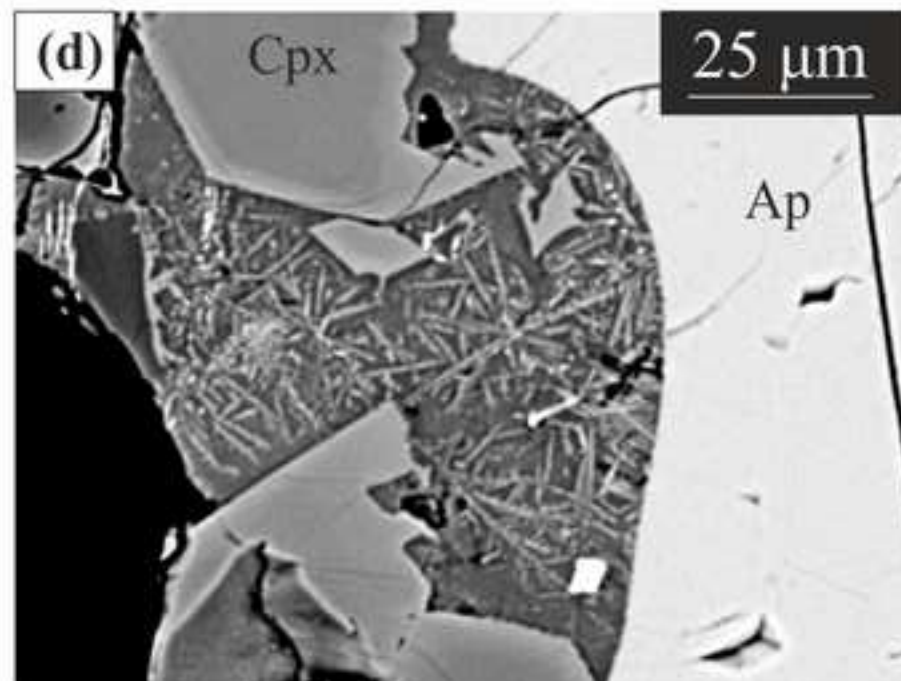
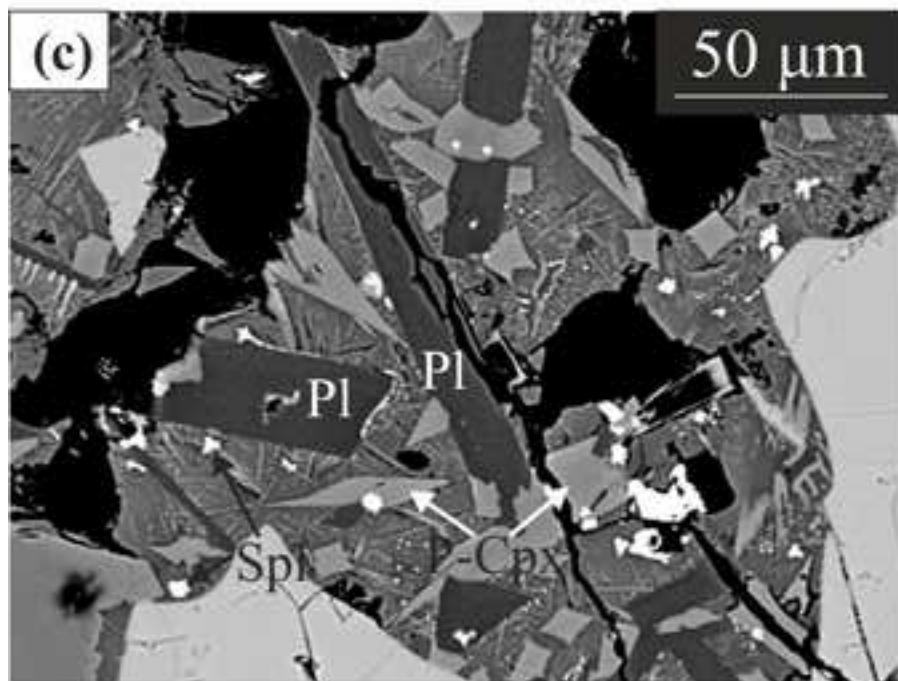
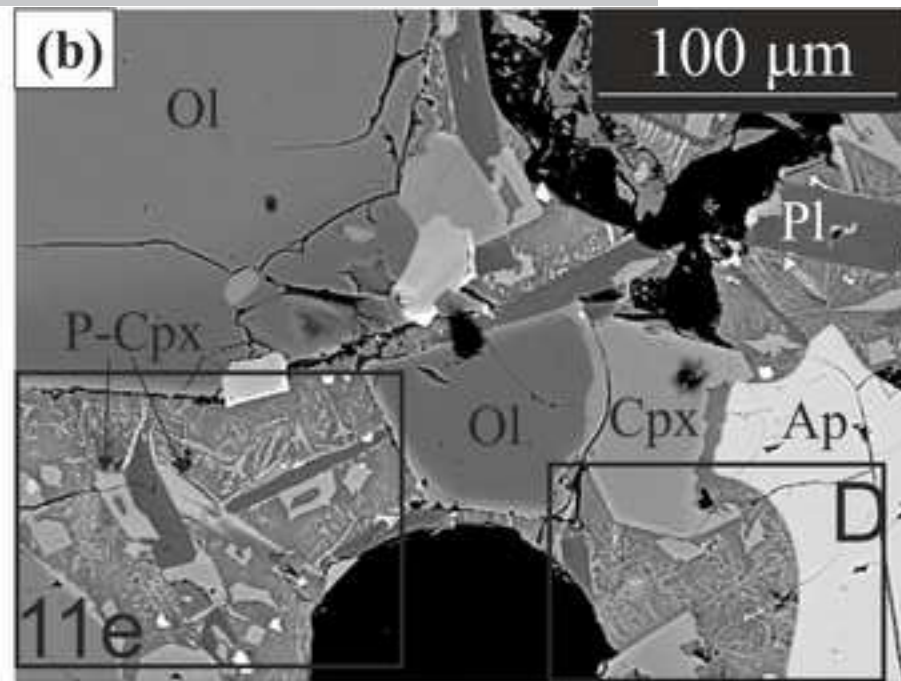
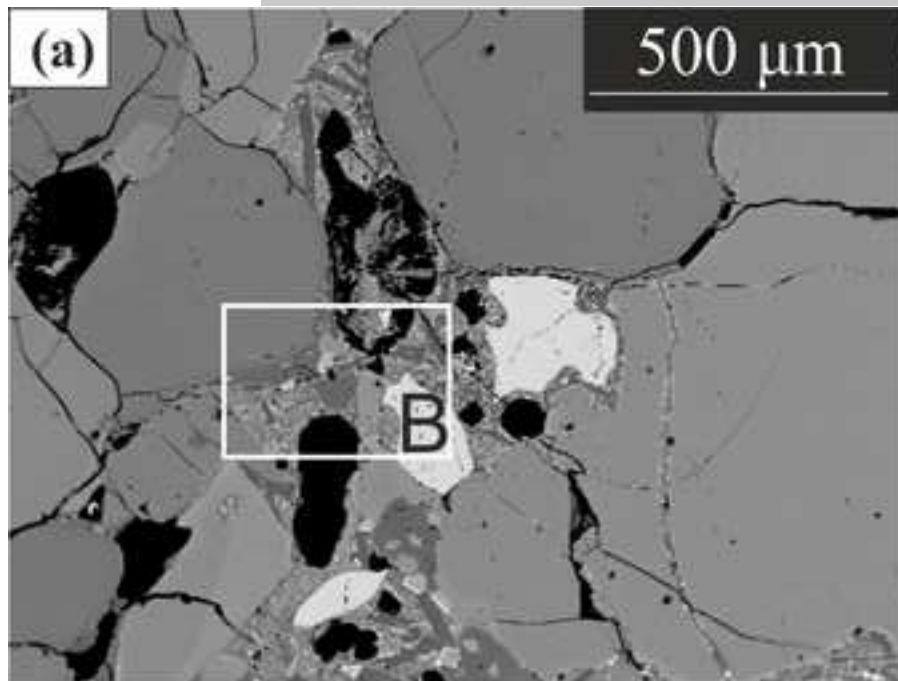
Appendix

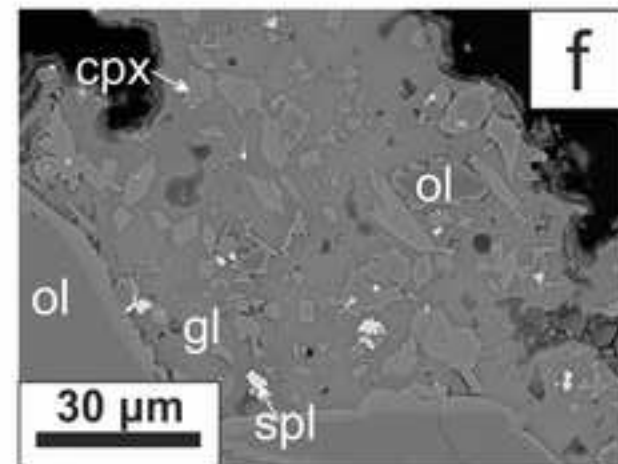
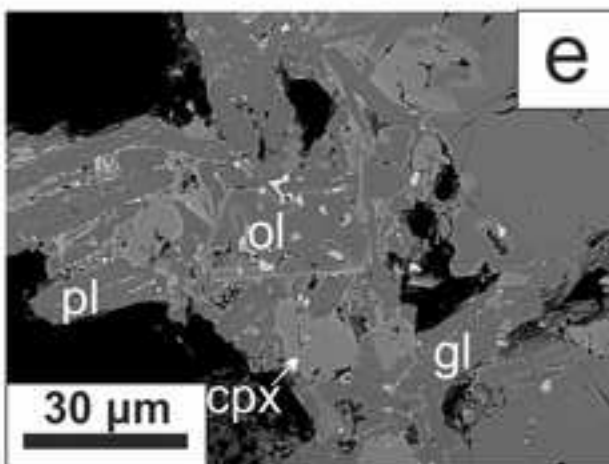
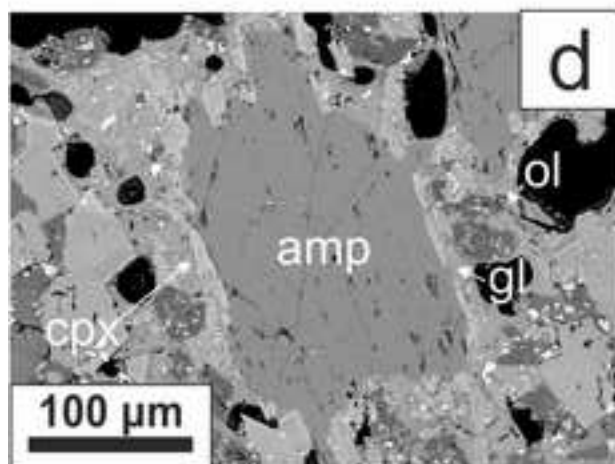
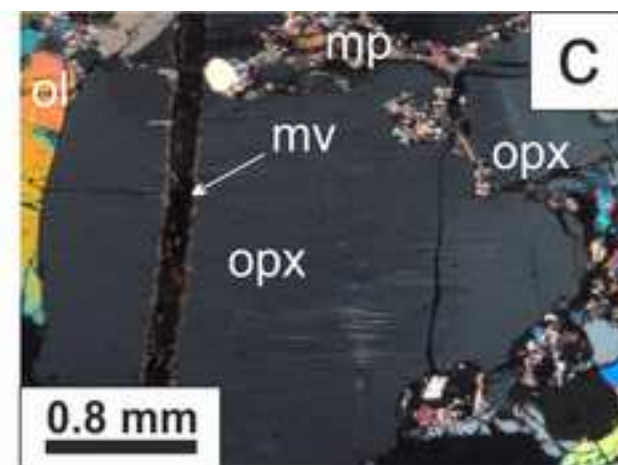
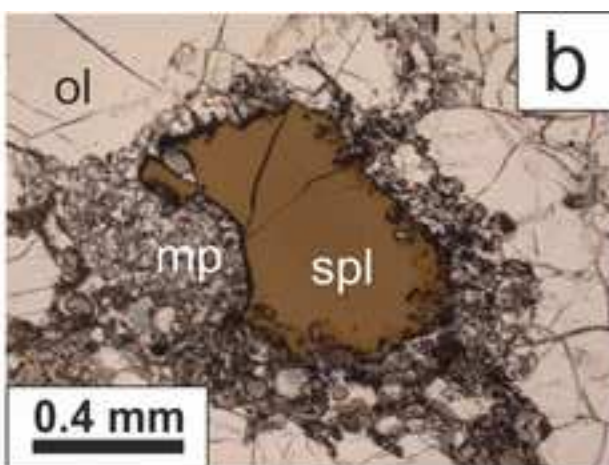
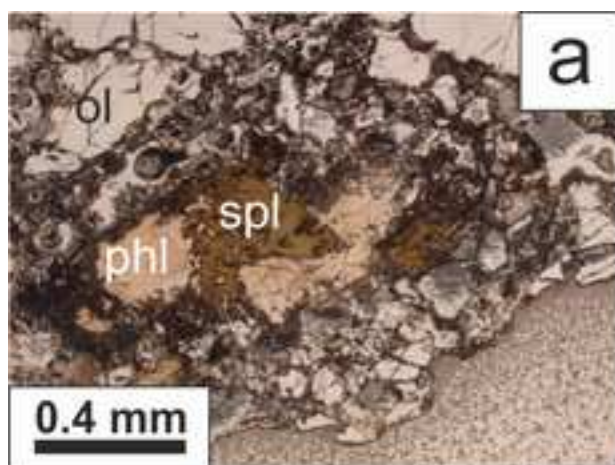
Figure S6. Sample Ci-1-105a. Lithologic boundaries are emphasized in the hand sample photograph and the location of the polished section is indicated by the white rectangle. The dark melt vein and melt pocket are indicated on the bottom most polished thin section mosaic.

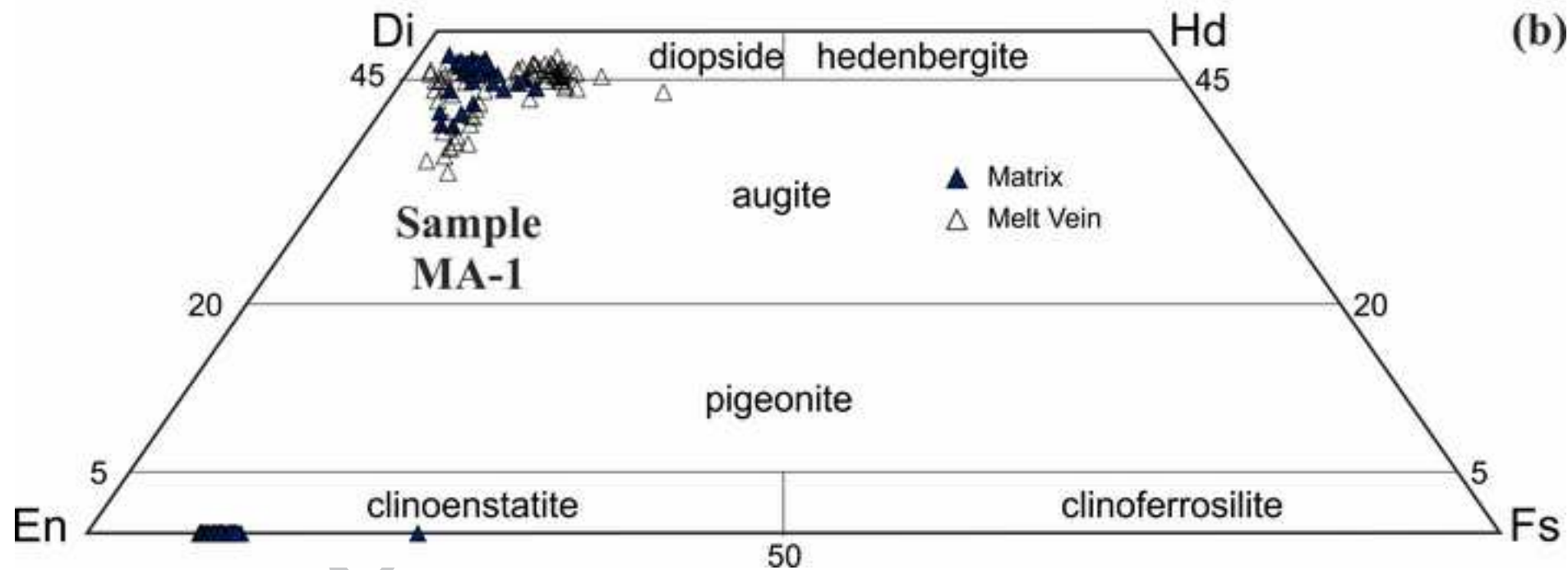
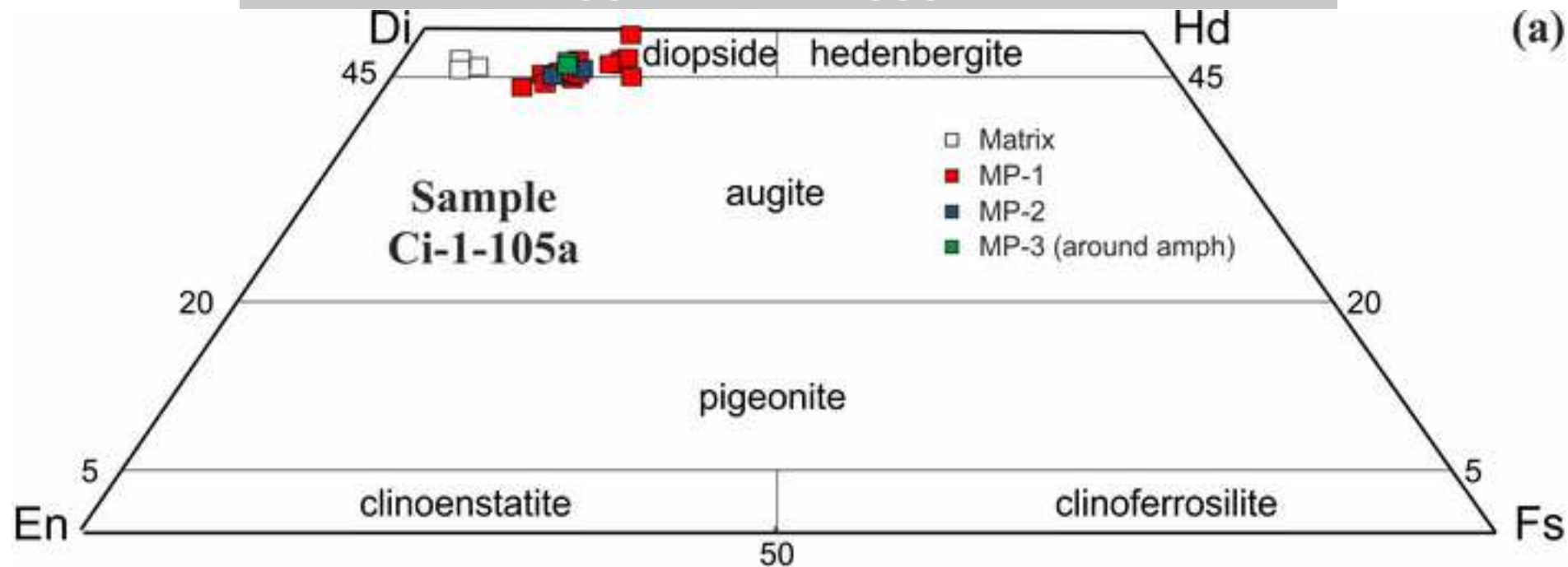
Figure S7. Sample MA-1. The analysed matrix and melt vein areas are indicated by rectangles defining the locations of the thin sections shown in figure 2.

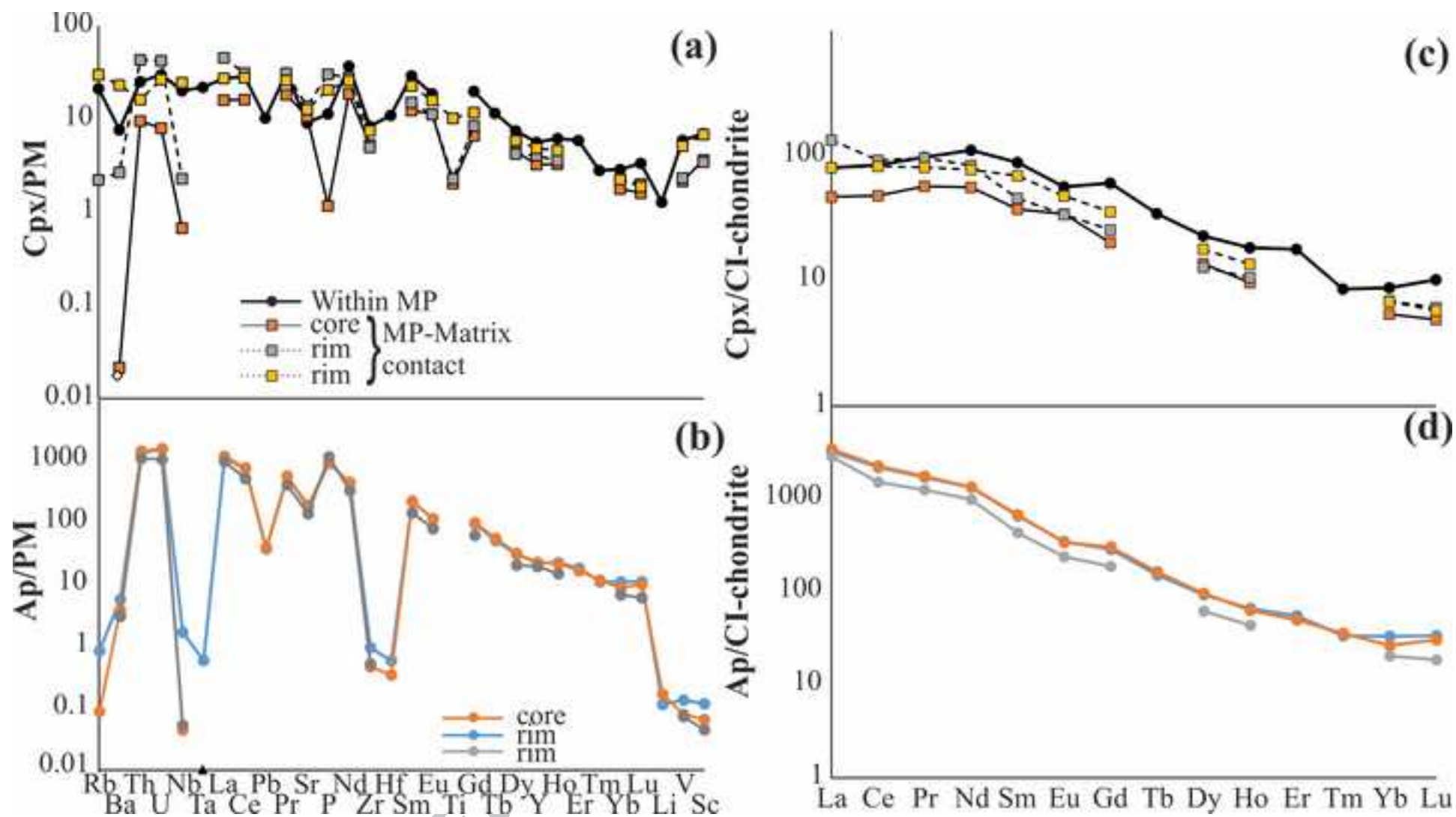
Figure S3. Total-alkali Silica (TAS) diagram doped with MELTS models at variable conditions (pressures 1, 33, 8 and 2 kbar; H_2O 0.1, 0.5 and 1.0 wt%; QFM -1 to +1). Abbreviations of glasses as in figure 6.

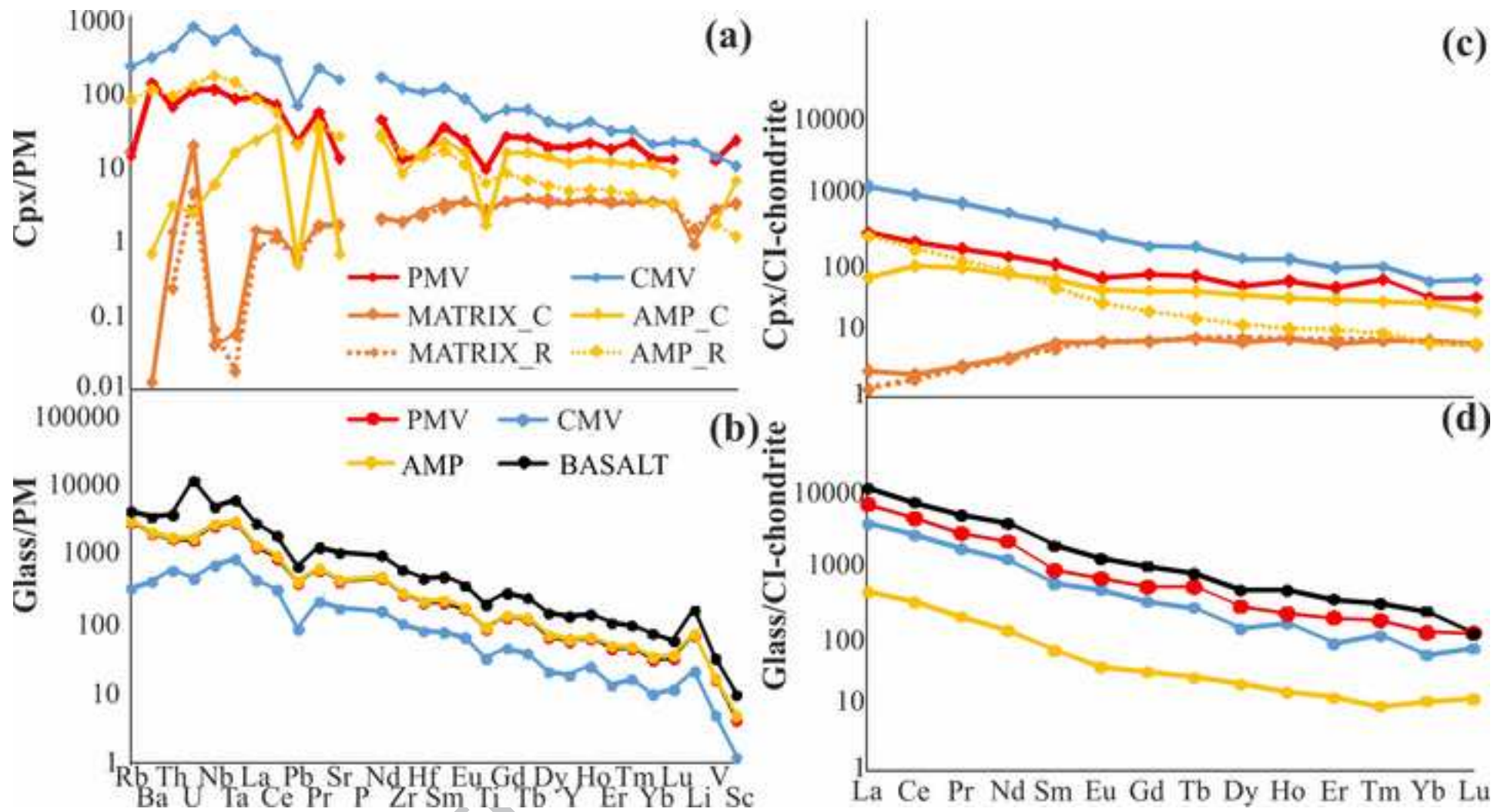
Figure S4. MgO (in wt%) variation diagrams for major oxides (in wt%) for glass analyses in sample MA-1 doped with MELTS models (as in figure S3). Abbreviations as in figure 6.

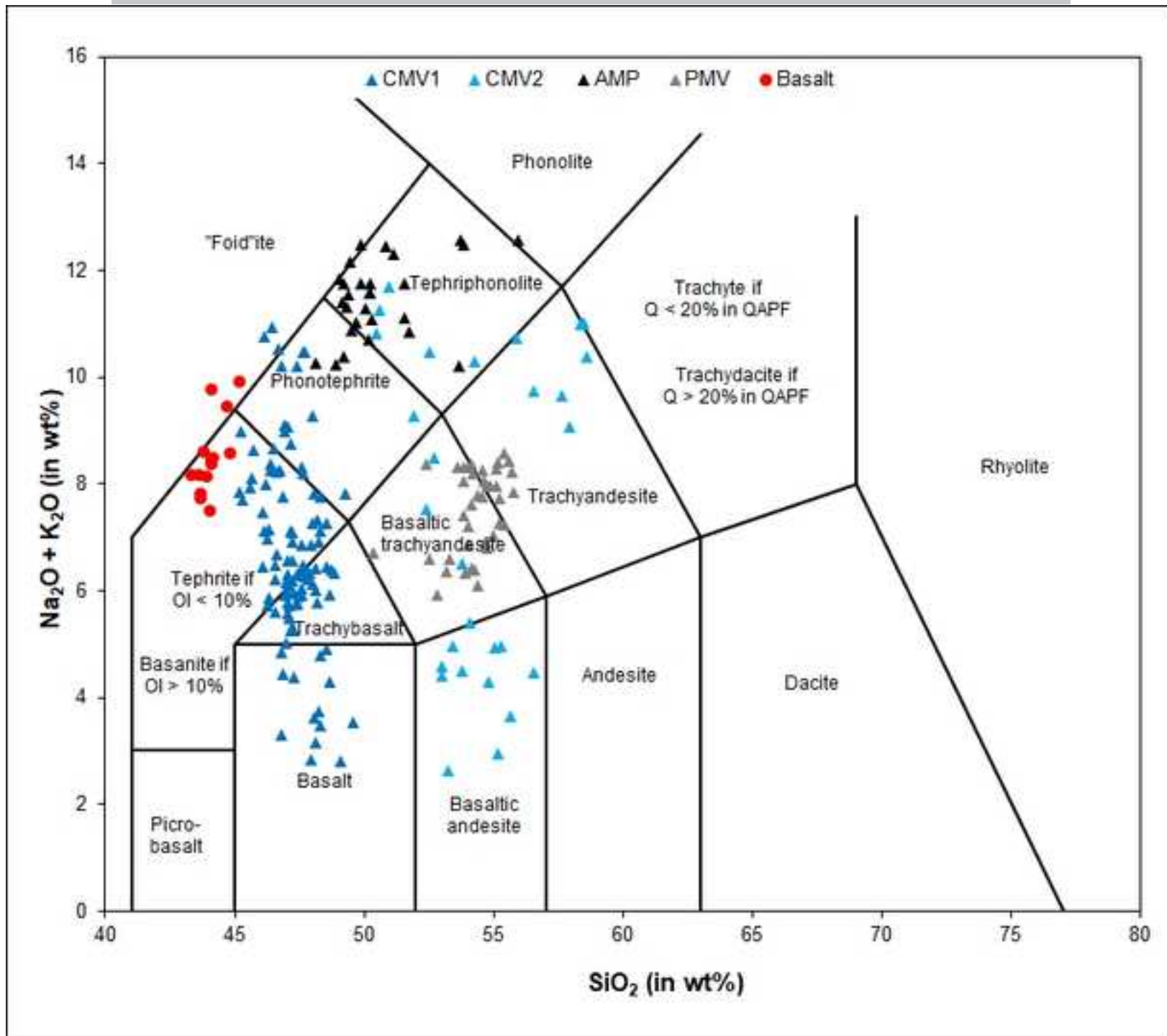


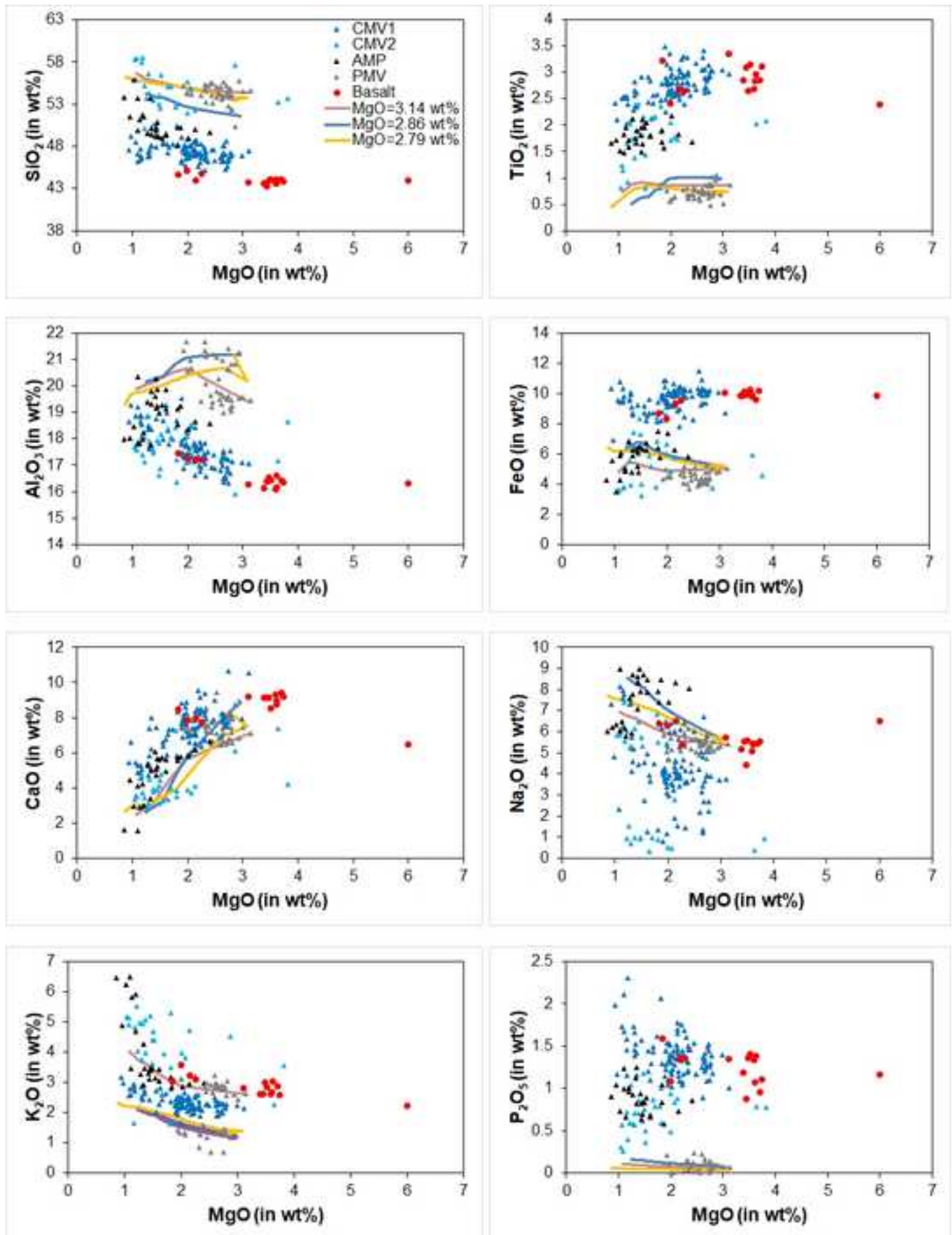


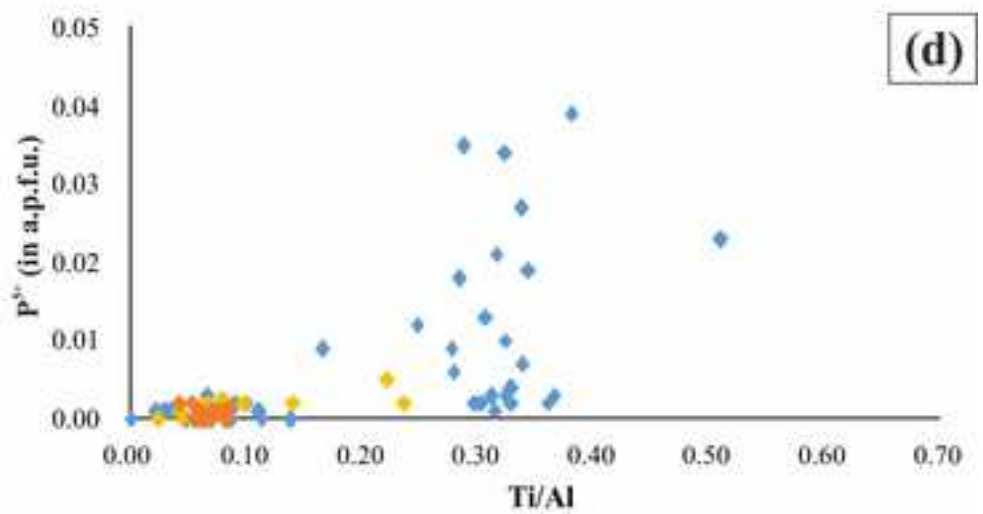
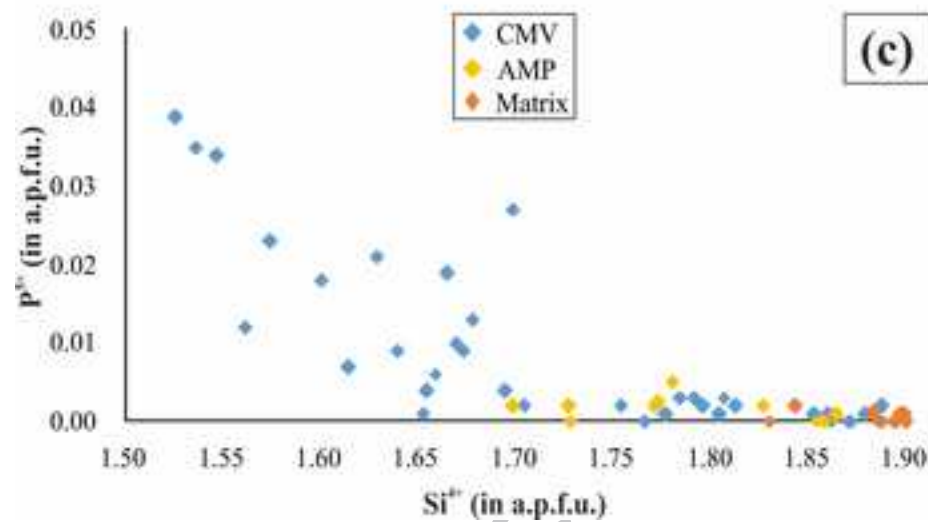
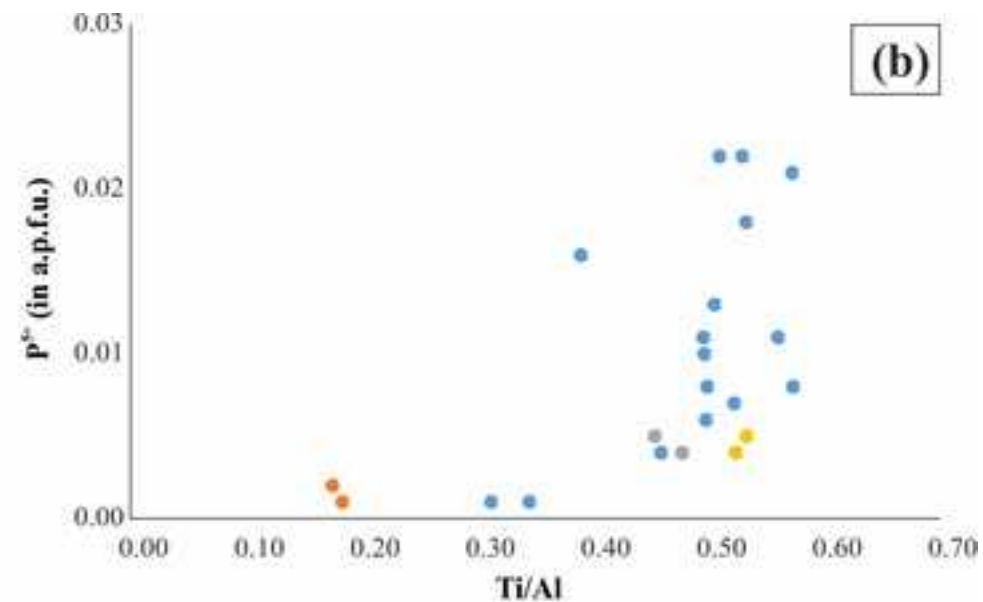
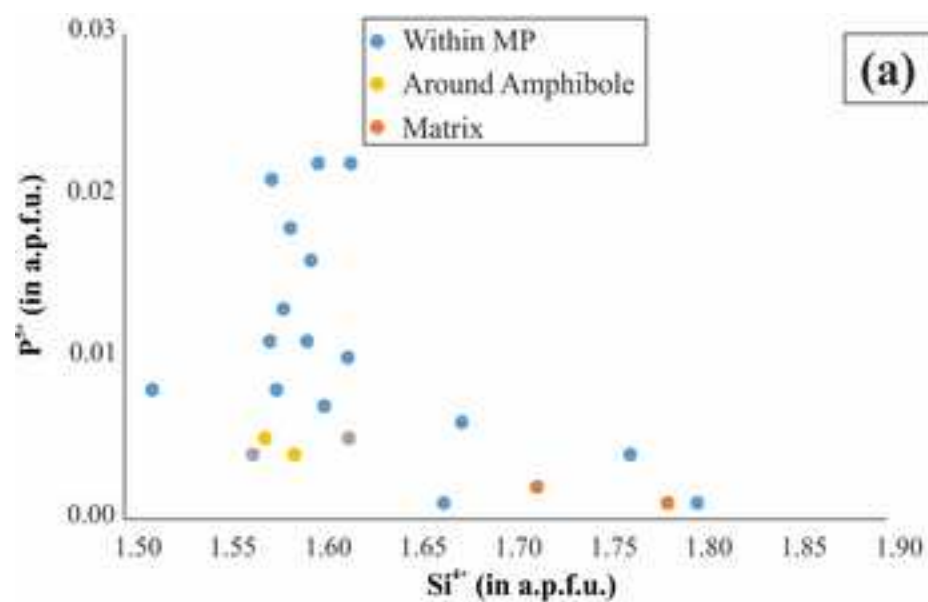


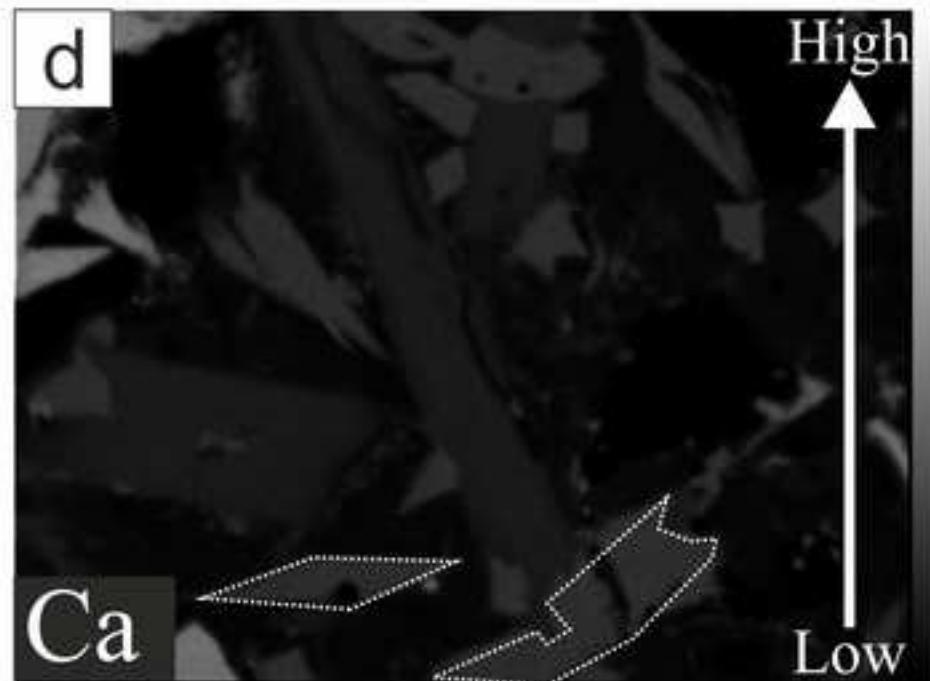
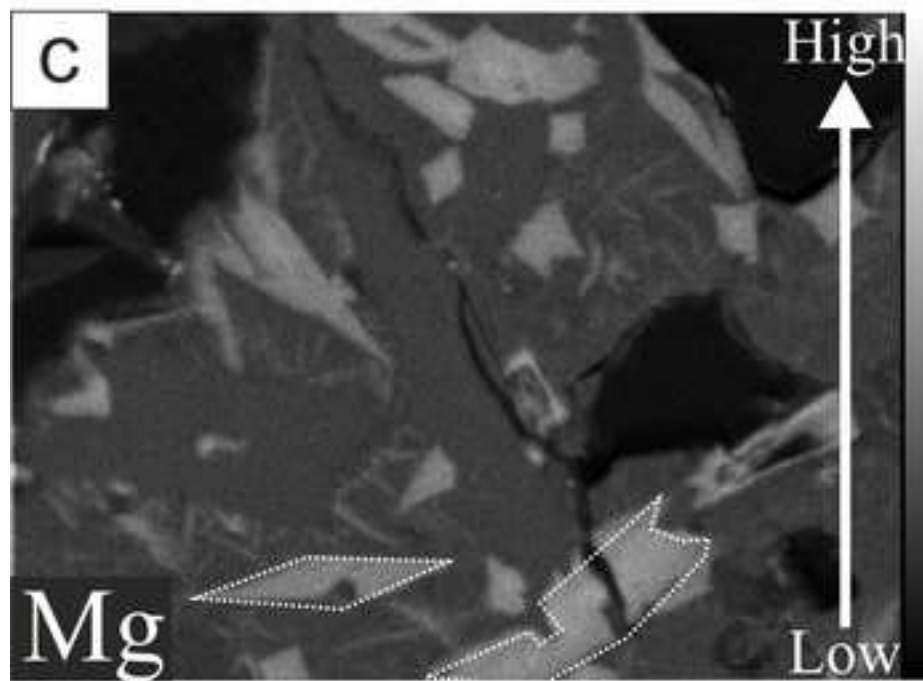
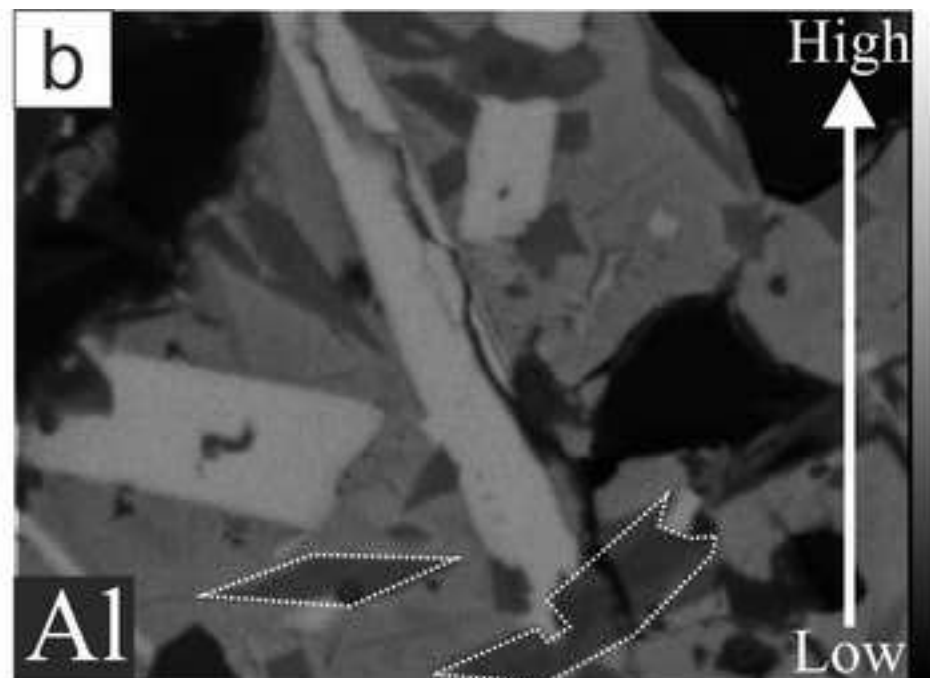
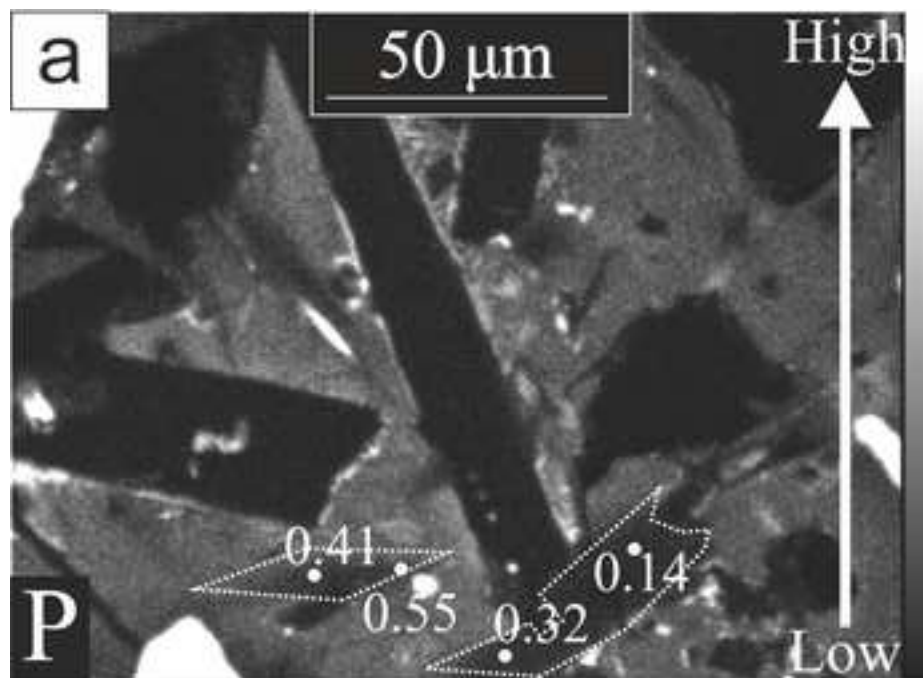


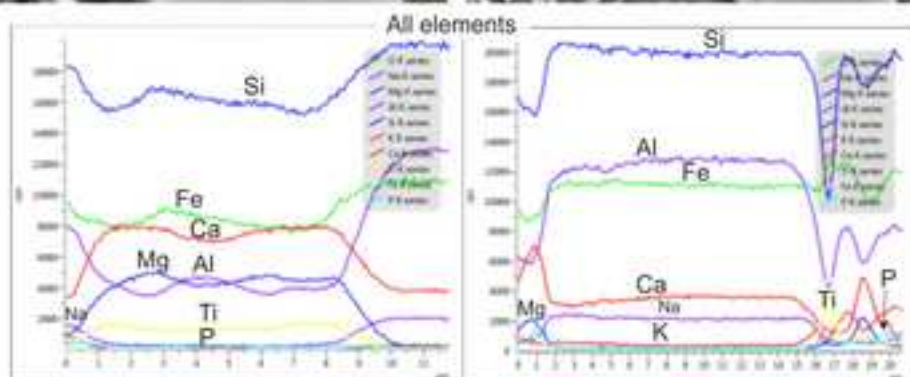
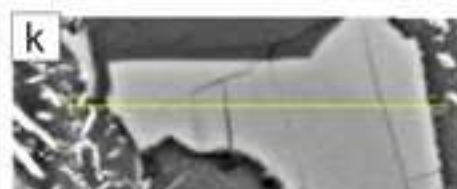
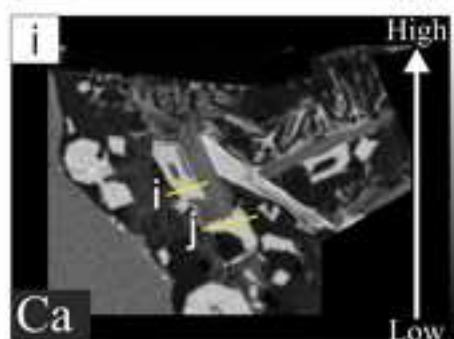
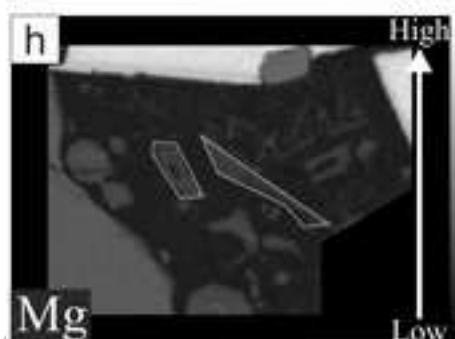
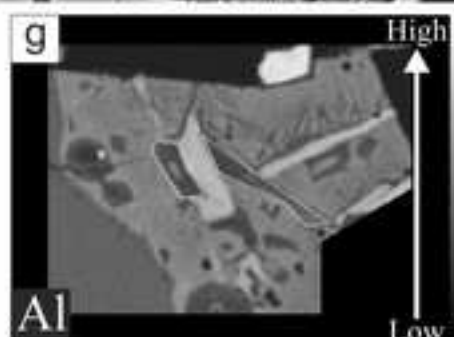
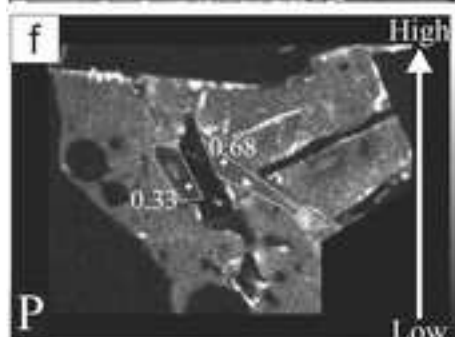
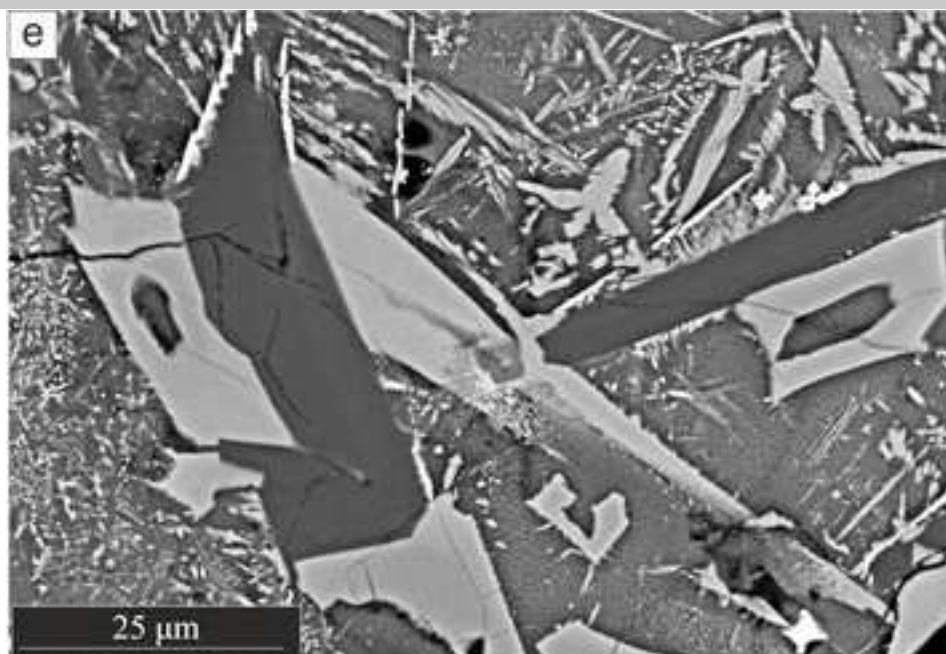


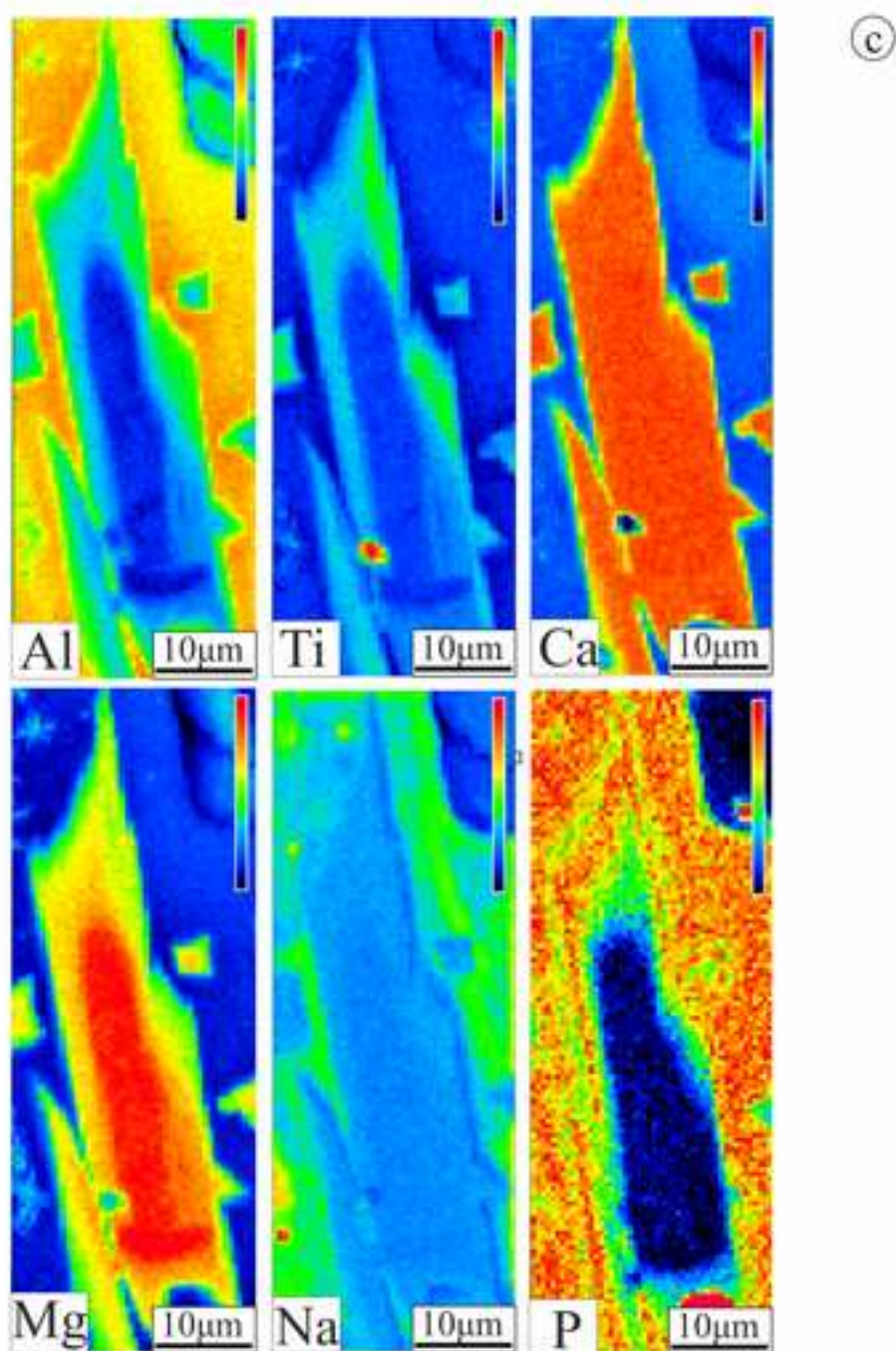
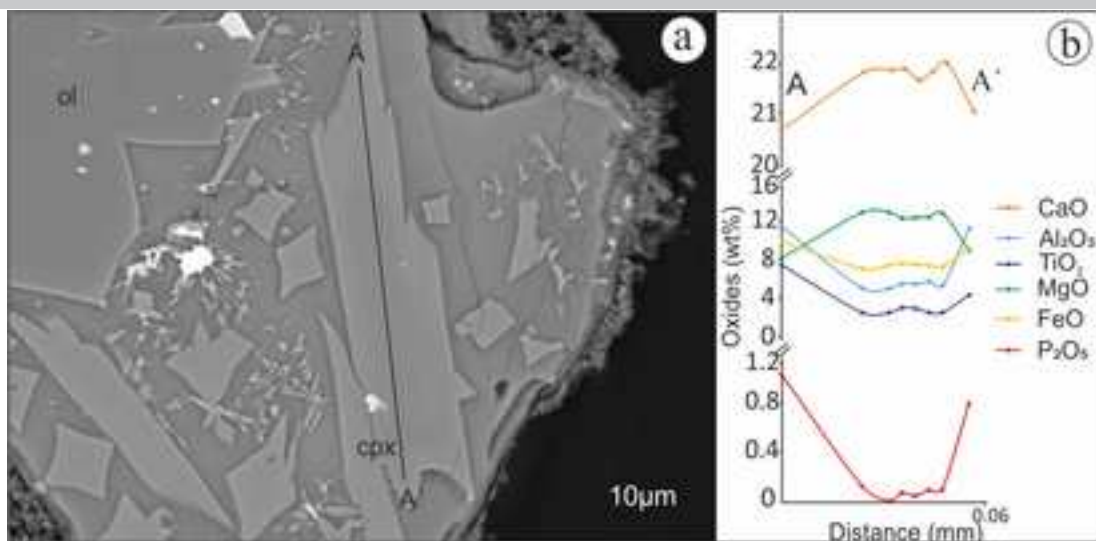




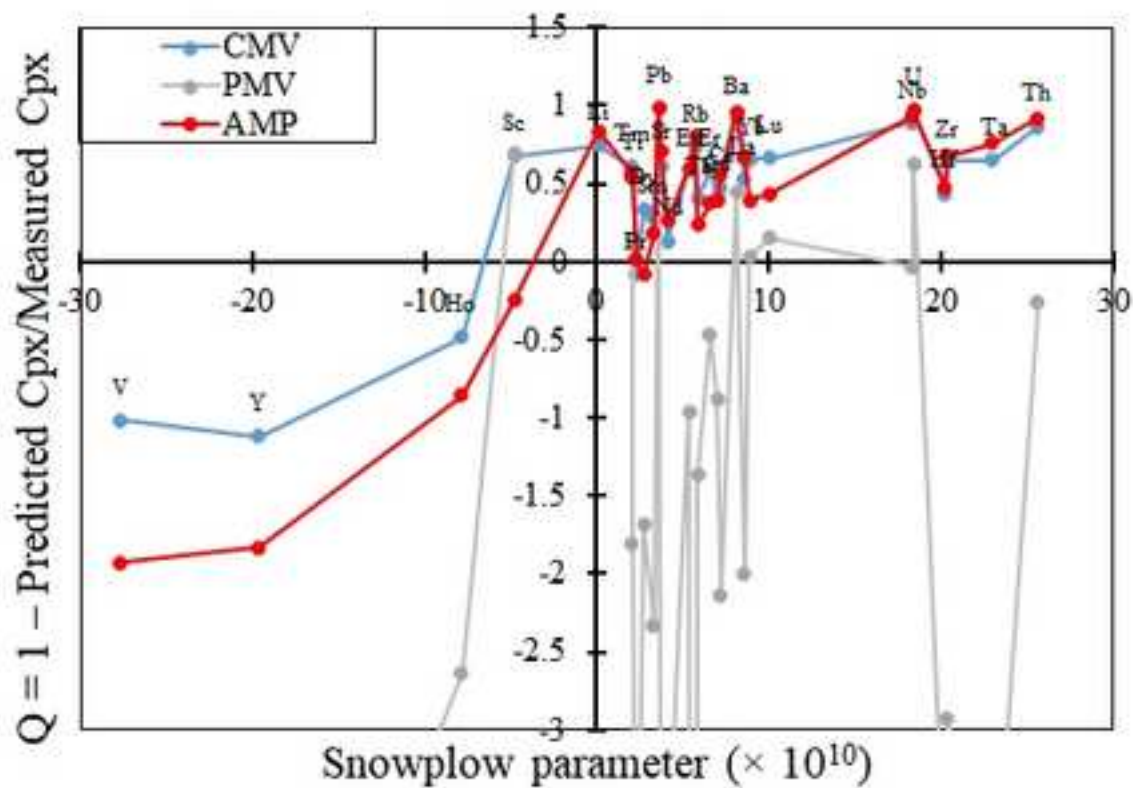








Alkali-Basalt



Basaltic-Andesite

(b)

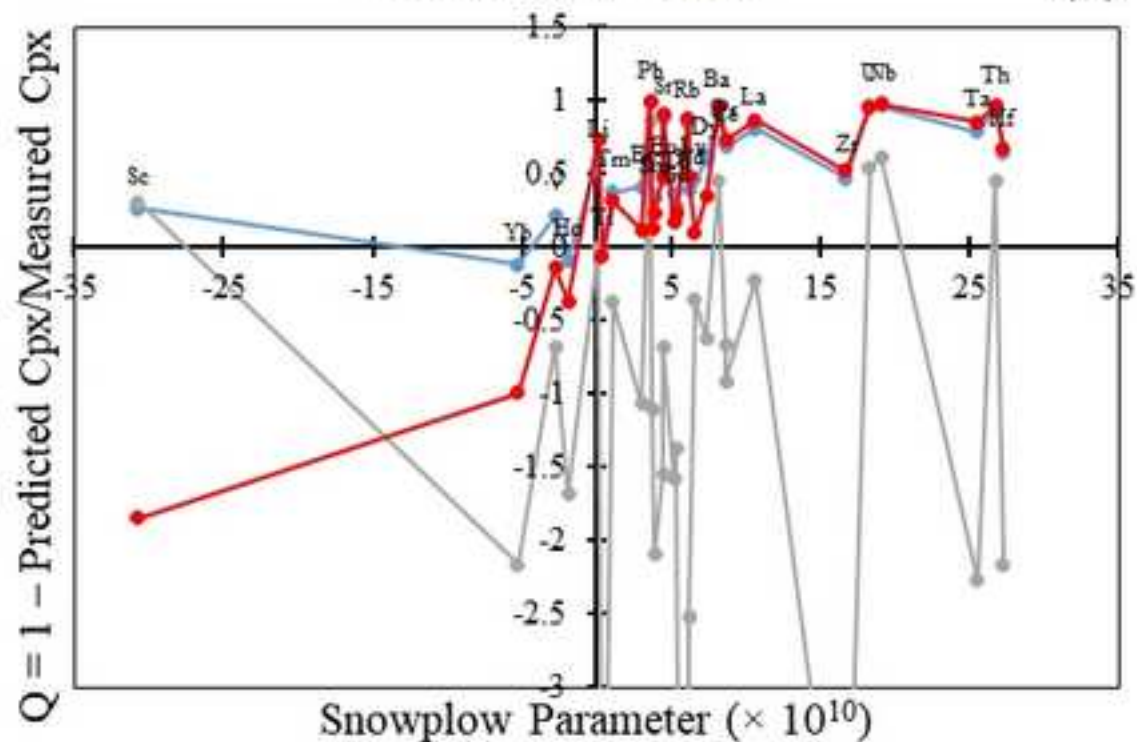


Table 1: Average major-element composition (wt%) of primary and secondary phases determined by EPMA for sample Ci-1-105a.

	ML		Matrix		MP		MP		Matrix		MP		Matrix					
	OI		OI		Gl		Cpx		Cpx		Pl		Spl					
	Mean	SD	Mean	SD	Mean	SD	Mean	SD	Mean	SD	Mean	SD	Mean	SD				
SiO ₂	40.5	0.45	40.1	0.23	SiO ₂	49.6	2.75	SiO ₂	42.8	2.56	47.2	1.16	SiO ₂	52.9	1.35	SiO ₂	0.07	0.00
TiO ₂			0.01	0.01	TiO ₂	2.79	0.84	TiO ₂	6.50	1.66	2.27	0.29	TiO ₂	0.31	0.10	TiO ₂	0.87	0.01
Al ₂ O ₃	0.04	0.02	0.02	0.01	Al ₂ O ₃	18.7	3.21	Al ₂ O ₃	9.22	2.33	8.26	1.33	Al ₂ O ₃	28.7	1.08	Al ₂ O ₃	51.6	0.12
Cr ₂ O ₃			0.01	0.02	Cr ₂ O ₃			Cr ₂ O ₃	0.23	0.37	0.96	0.20	FeO	0.60	0.07	Cr ₂ O ₃	12.2	0.33
FeO	12.1	2.25	14.0	1.14	FeO	6.48	0.96	FeO	7.01	1.11	3.57	0.22	MgO	0.12	0.03	FeO	13.8	0.50
MnO	0.15	0.05	0.19	0.03	MgO	1.68	1.90	MnO	0.13	0.02	0.06	0.01	CaO	11.8	1.24	MnO	0.07	0.01
MgO	46.3	1.66	45.0	0.96	CaO	5.81	5.41	MgO	10.8	1.71	14.0	0.74	Na ₂ O	4.23	0.50	MgO	20.3	0.18
CaO	0.19	0.09	0.11	0.05	Na ₂ O	4.54	2.41	CaO	21.2	1.38	22.7	0.24	K ₂ O	0.75	0.20	CaO	0.02	0.02
NiO	0.29	0.03	0.27	0.02	K ₂ O	6.07	2.57	Na ₂ O	0.78	0.42	0.44	0.01	Total	99.5		NiO	0.34	0.03
P ₂ O ₅	0.07	0.03	0.05	0.02	P ₂ O ₅	1.33	0.48	K ₂ O	0.14	0.24	0.01	0.01	<i>n</i>	3		ZnO	0.07	0.02
Total	99.6		99.8		SO ₂	0.13	0.02	NiO	0.02	0.02	0.04	0.01				Total	99.4	
<i>n</i>	3		58		Total	97.2		P ₂ O ₅	0.32	0.26	0.03	0.03				<i>n</i>	2	
					<i>n</i>	4		Total	99.0		99.6							
								<i>n</i>	22		3							

Abbreviations: ML: melt layer; MP: melt pocket; Ol: olivine; Gl: glass; Cpx: clinopyroxene; Pl: plagioclase; Spl: spinel.

Table 2: Average major-element composition (wt%) of primary and secondary phases determined by EPMA for sample MA-1

	PMV		CMV		AMP		Matrix		PMV		CMV		AMP		Matrix	
	Ol		Ol		Ol		Ol		Cpx		Cpx		Cpx		Cpx	
	Mean	SD	Mean	SD	Mean	SD	Mean	SD	Mean	SD	Mean	SD	Mean	SD	Mean	SD
SiO ₂	40.5	0.54	39.7	0.84	41.4	0.25	40.6	0.23	48.8	3.55	47.3	4.80	49.1	2.39	52.2	0.58
TiO ₂	0.02	0.02	0.05	0.03	0.03	0.02	0.01	0.02	1.79	1.78	2.39	2.20	1.00	0.77	0.67	0.09
Al ₂ O ₃	0.08	0.17	0.10	0.10	0.07	0.03	0.01	0.01	6.37	1.96	6.60	2.72	6.72	2.09	6.30	0.66
Cr ₂ O ₃	0.06	0.06	0.04	0.03	0.13	0.07	0.01	0.01	0.74	0.78	0.42	0.50	1.30	0.72	0.64	0.20
FeO	9.55	2.23	13.8	2.81	6.64	0.90	10.5	0.18	5.31	2.12	6.17	2.26	4.69	1.08	2.67	0.24
MnO	0.16	0.05	0.25	0.06	0.16	0.02	0.16	0.03	0.12	0.03	0.13	0.03	0.12	0.03	0.08	0.03
MgO	49.0	2.26	45.0	2.76	51.7	0.79	48.7	0.29	14.8	2.26	13.9	3.15	14.7	1.76	14.5	0.43
CaO	0.17	0.09	0.26	0.09	0.29	0.03	0.03	0.02	20.2	1.40	20.3	1.08	21.3	1.10	20.6	0.38
Na ₂ O			0.04	0.03					0.74	0.40	0.68	0.34	0.61	0.29	1.78	0.20
K ₂ O			0.03	0.03					0.02	0.03	0.04	0.02	0.02	0.02	0.01	0.01
NiO	0.35	0.06	0.19	0.09	0.33	0.06	0.35	0.03	0.03	0.03	0.04	0.03	0.04	0.02	0.03	0.02
P ₂ O ₅	0.04	0.07	0.20	0.19	0.02	0.03	0.01	0.02	0.11	0.20	0.26	0.43	0.04	0.02	0.02	0.02
Total	99.9	0.35	99.5	0.86	100.7	0.30	100.3	0.30	99.0	0.50	98.3	0.88	99.7	0.37	99.6	0.37
<i>n</i>		14		55		11		61		26		26		12		39

Abbreviations: PMV: parallel melt vein; CMV: cross-cutting melt vein; AMP: amphibole melt pocket; Ol: olivine; Cpx: clinopyroxene.

Table 3: Average major-element composition (wt%) of glass and amphibole determined by EPMA for sample MA-1

	PMV		CMV		AMP		Host basalt		AMP	
	GI		GI		GI		GI		Amp	
	Mean	SD	Mean	SD	Mean	SD	Mean	SD	Mean	SD
SiO ₂	54.0	1.26	48.8	3.23	49.6	0.61	44.1	0.47	44.5	0.13
TiO ₂	0.89	0.39	2.53	0.55	1.82	0.20	2.88	0.28	0.38	0.05
Al ₂ O ₃	19.8	1.12	17.7	0.71	19.3	0.54	16.6	0.44	12.6	0.21
Cr ₂ O ₃	0.06	0.04	0.05	0.03	0.02	0.02	0.02	0.02	1.48	0.09
FeO	4.45	0.48	8.73	2.01	6.25	0.62	9.73	0.52	5.26	0.06
MnO	0.09	0.06	0.18	0.07	0.12	0.04	0.19	0.05	0.11	0.01
MgO	2.30	0.61	1.98	0.56	1.61	0.32	3.28	0.98	18.0	0.08
CaO	6.56	1.17	6.69	1.76	5.48	0.56	8.65	0.78	10.2	0.11
Na ₂ O	5.49	0.43	4.16	1.87	8.16	0.54	5.65	0.56	3.92	0.06
K ₂ O	2.74	1.54	2.74	0.91	3.20	0.23	2.88	0.32	0.41	0.02
NiO	0.07	0.05	0.06	0.04	0.02	0.02	0.03	0.03	0.10	0.02
P ₂ O ₅	0.27	0.37	1.23	0.38	0.85	0.17	1.24	0.19	0.02	0.01
Total	96.8	1.48	94.8	1.51	96.4	0.57	95.2	0.61	97.00	0.31

<i>n</i>	47	132	19	15	7
Abbreviations: PMV: parallel melt vein; CMV: cross-cutting melt vein; amphibole melt pocket; Gl: glass; Amp: amphibole.					

ACCEPTED MANUSCRIPT

Table 4: Average trace-element composition of primary and secondary phases determined by LA-ICP-MS for sample Ci-1-105a

	MP			Matrix			MP			MP			MP			MP		
	OI			OI			Cpx P-Cr-poor			Cpx Cr-poor P Ti-rich			Cpx P-Cr-rich			Ap		
	Mean	SD	n	Mean	SD	n	Single	SD	n	Mean	SD	n	Single	SD	n	Mean	SD	n
Rb	0.01	-	1	5.06	6.88	5	-	-	-	10.2	12.5	2	13.6	-	-	0.29	0.34	2
Ba	0.96	0.11	2	41.9	76.8	8	0.15	-	-	90.8	101.8	2	53.7	-	-	29.0	9.42	3
Th	0.06	0.03	2	0.35	0.69	9	0.82	-	-	2.54	1.64	2	2.15	-	-	105.0	15.0	3
U	0.07	-	1	0.12	0.19	8	0.17	-	-	0.73	0.23	2	0.63	-	-	28.1	5.85	3
Nb	n.d.	-	0	4.26	9.66	9	0.48	-	-	9.65	11.3	2	14.4	-	-	0.42	0.67	3
Ta	0.02	0.02	2	0.01	-	1	0.00	-	-				0.90	-	-	0.01	0.02	2
La	0.13	0.15	2	3.66	6.53	8	11.0	-	-	25.0	8.82	2	18.8	-	-	720	70.0	3
Ce	0.05	0.07	2	5.73	11.4	10	28.9	-	-	52.50	4.20	2	51.1	-	-	1160	240.0	3
Pb	0.42	-	1	0.24	0.30	2	0.00	-	-				1.91	-	-	6.97	0.26	2
Pr	0.02	0.02	2	1.06	1.65	7	5.07	-	-	7.91	0.98	2	8.67	-	-	135.0	25.0	3
Sr	1.57	-	1	32.4	64.5	9	225.0	-	-	280.0	15.5	2	193.0	-	-	3465	545.0	3
P	165.0	70.0	3	410.0	405.0	11	110.0	-	-	2430	650.0	2	1084	-	-	91600	13400	3
Nd	0.19	-	1	4.34	7.19	7	25.4	-	-	36.5	2.01	2	50.2	-	-	535.0	88.0	3
Zr	0.56	-	1	15.8	35.3	8	59.8	-	-	70.0	19.9	2	93.7	-	-	7.19	2.99	3
Hf	0.06	0.06	2	0.06	-	1	-	-	-				3.41	-	-	0.14	0.05	2
Sm	0.13	0.09	2	1.16	1.83	5	5.51	-	-	8.44	2.45	2	13.0	-	-	84.4	19.3	3
Eu	n.d.	-	0	0.20	0.39	8	1.91	-	-	2.29	0.55	2	3.16	-	-	16.9	3.31	3
Ti	22.8	-	1	943.0	1730	9	2650	-	-	8150	7310	2		-	-	n.d.	-	-
Gd	0.12	0.13	2	0.95	1.51	5	3.97	-	-	6.02	1.39	2	11.9	-	-	49.9	12.0	3

Tb	0.06	-	1	0.01	-	2	-	-	-			1.25	-	-	5.63	0.32	2	
Dy	n.d.	-	0	0.49	0.80	7	3.33	-	-	3.74	0.87	2	5.54	-	-	20.0	4.49	3
Y	0.07	0.02	2	1.59	3.51	9	14.8	-	-	20.3	2.58	2	25.7	-	-	95.7	8.02	3
Ho	n.d.	-	0	0.11	0.18	7	0.54	-	-	0.67	0.12	2	1.02	-	-	3.16	0.67	3
Er	0.13	-	1	n.d.	-	0	-	-	-				2.84	-	-	8.24	0.63	2
Tm	0.07	0.06	2	0.06	-	1	-	-	-				0.21	-	-	0.83	0.04	2
Yb	0.07	0.05	2	0.20	0.37	7	0.88	-	-	1.12	0.01	2	1.43	-	-	4.28	1.02	3
Lu	0.01	0.01	2	0.07	0.08	5	0.12	-	-	0.14	0.01	2	0.25	-	-	0.66	0.19	3
Li	4.73	0.66	3	4.54	0.71	2	-	-	-				2.06	-	-	0.23	0.06	2
V	4.03	2.88	3	26.9	43.8	11	175.0	-	-	310.0	160.0	2	485.7	-	-	7.82	2.77	3
Sc	3.58	2.36	3	4.75	2.93	11	62.4	-	-	87.9	40.8	2	119.4	-	-	1.29	0.64	3
B	1.47	0.12	2	1.39	-	3	-	-	-				2.18	-	-	1.28	1.07	2
Ni	2190	80.0	2	2200	230.0	3	305.0	-	-	445.0	160.0	2	250.0	-	-	2.30	1.82	3
Cr	88.0	86.0	2	110.0	50.0	3	175.0	-	-	310.0	165.0	2	9400	-	-	n.d.	-	-

n.d. not determined; Abbreviations: MP: melt pocket; Ol: olivine; Cpx: clinopyroxene; Ap: apatite.

Table 5: Trace-element composition of olivine and clinopyroxene determined by LA-ICP-MS for sample MA-1

	PMV	CMV	Matrix	PMV	CMV	Matrix	Matrix
	OI	OI	OI	Cpx	Cpx	Cpx-core	Cpx-rim
	Mean	Mean	Single	Single	Single	Single	Single
Rb	0.30	0.26	0.05	10.6	155.0	n.d.	n.d.
Ba	3.17	3.80	16.6	1060	2290	n.d.	0.14
Th	0.07	0.01	0.003	6.29	37.4	0.03	0.15
U	0.02	0.002	0.001	2.53	17.5	0.12	0.50
Nb	0.68	0.37	0.01	90.0	385.0	0.07	0.04
Ta	0.04	0.03	0.05	3.87	30.4	0.001	0.003
La	0.38	0.04	0.03	69.8	266.4	0.75	1.27
Ce	0.52	0.30	0.24	140.0	550.0	2.56	3.01
Pb	0.86	0.04	0.01	4.68	14.3	0.14	0.16
Pr	0.05	0.01	0.48	17.7	66.7	0.56	0.60
Sr	2.77	0.69	0.05	335.0	3550	44.8	46.3
Nd	0.13	0.03	0.01	69.2	245.0	3.44	3.67
Zr	1.06	3.68	n.d.	175.0	1460	26.0	26.5
Hf	0.02	0.03	n.d.	5.29	36.1	0.86	1.00
Sm	0.03	0.01	n.d.	18.1	58.8	1.56	1.85
Eu	0.02	0.01	n.d.	4.59	16.1	0.73	0.74
Ti	30.1	47.2	2.67	14950	69200	4230	4480

Gd	n.d.	n.d.	0.01	18.4	40.8	2.53	2.64
Tb	0.01	n.d.	0.001	3.17	7.4	0.51	0.51
Dy	0.04	0.001	n.d.	16.2	35.7	3.49	3.11
Y	0.20	0.04	0.04	102.0	185.0	19.4	19.4
Ho	n.d.	0.003	n.d.	4.15	7.9	0.75	0.79
Er	0.02	0.01	0.003	9.95	17.5	2.16	1.96
Tm	0.005	n.d.	0.001	1.89	2.73	0.32	0.32
Yb	0.05	0.01	0.01	7.68	12.1	2.08	2.21
Lu	0.003	n.d.	n.d.	1.15	1.93	0.29	0.31
Li	3.58	1.45	4.69	n.d.	40.8	3.02	1.91
V	2.78	0.99	2.22	1200	1400	280.0	285.0
Sc	3.47	1.21	1.38	465.0	215.0	68.5	71.5

n.d.: not determined;

Abbreviations: PMV: parallel melt vein; CMV: cross-cutting melt vein; Ol: olivine; Cpx: clinopyroxene.

Table 6: Trace-element composition of glass and amphibole determined by LA-ICP-MS for sample MA-1

	PMV	CMV	MI	Matrix	Matrix	Host basalt
	GI	GI	GI	Amp-core	Amp-rim	GI
	Mean	Mean	Single	Single	Single	Single
Rb	1940	305.0	220.0	1.10	54.2	805.0
Ba	13300	4220	1450	6.38	890.0	10550
Th	115.0	70.6	18.4	0.33	8.71	180.7
U	29.4	13.8	5.26	0.06	3.02	210.6
Nb	1550	690.0	220.0	5.21	135.0	1588
Ta	93.2	48.3	12.8	0.78	6.43	130.0
La	726	430.0	120.0	18.9	63.5	1107
Ce	1290	836.9	225.0	68.8	110.0	1965
Pb	78.8	26.5	18.8	0.12	4.49	64.1
Pr	135.0	90.6	26.6	9.98	12.2	220.0
Sr	6950	5640	980.0	19.0	645.0	16300
Nd	540.0	340.0	90.8	41.3	45.0	870.0
Zr	2550	1922	450.0	115.0	220.0	4850
Hf	55.7	42.2	9.84	5.84	5.01	99.7
Sm	83.0	58.6	17.4	11.5	8.91	157.6
Eu	25.4	18.9	5.22	3.26	2.22	42.2
Ti	108000	78500	19400	2800	9800	195000

Gd	71.8	49.1	16.2	11.3	6.11	125.0
Tb	13.1	7.6	2.39	2.02	0.91	18.4
Dy	53.6	29.4	12.4	12.4	5.19	82.5
Y	295.0	165.0	61.6	62.9	27.0	465.0
Ho	9.88	7.65	2.31	2.54	1.02	18.1
Er	25.7	12.9	5.01	6.89	2.88	41.7
Tm	3.62	2.39	0.66	0.99	0.39	5.60
Yb	18.0	10.0	5.01	6.40	2.01	31.4
Lu	2.66	1.77	0.71	0.76	0.30	2.61
Li	125.0	65.2	19.0	9.06	11.0	205.0
V	1670	910.0	380.0	175.0	185.0	2205
Sc	108.2	53.1	67.3	140.0	26.0	158.5

Abbreviations: PMV: parallel melt vein; CMV: cross-cutting melt vein; MI: melt inclusion; Gl: glass; Amp: amphibole.

Table 7: The two adopted sets of clinopyroxene/melt K_d values

	Alkali basalt	Basaltic andesite		Alkali basalt	Basaltic andesite
U	0.032 ^{a,b,d}	0.04 ⁱ	Ho	1.53 ^{b,d}	1.128 ⁱ
P	0.021267	0.021267 ^{q,r}	Y	2.39 ^b	0.736 ^{f,j}
V	3.1 ^d	1.21 ^{h,i}	Dy	0.8115 ^{b,c,d,e}	0.489833 ^{m,v,u}
Nb	0.06 ^{b,d}	0.02235 ^{m,s,t,u,v}	Gd	0.4805 ^{c,d,e}	0.606667 ^{h,j}
Ta	0.22 ^{a,b,d}	0.136 ^y	Eu	0.354 ^{a,c}	0.46 ^{h,i}
Ti	0.388857 ^f	0.9 ^f	Sm	0.727 ^{b,c,d}	0.675 ^{f,h,i,j}
Hf	0.48 ^{a,b,d,e}	0.3 ⁱ	Tm	0.449 ^d	0.7184 ^{l,o,p}
Zr	0.27 ^{a,b,d,e}	0.4 ^f	Nd	0.6335 ^{b,c,d,e}	0.45 ^{f,h}
Th	0.07 ^{a,b,d}	0.03 ⁱ	La	0.288 ^{a,b,c,d,e}	0.1174 ^{f,i,j}
Pr	0.79 ^{b,d}	0.214333 ^p	Tb	0.575 ^{a,d}	0.625 ⁱ
Ce	0.341 ^{b,c,d,e}	0.208 ^{f,h,i}	Pb	0.008287	0.008287 ^{m,n}
Sc	1.31 ^{a,d}	2.9825 ^{j,k}	Sr	0.239 ^{b,c}	0.081067 ^{l,g}
Lu	0.365 ^{c,d,e}	0.5875 ^j	Ba	0.044 ^{a,b,c,d}	0.04383 ^{g,h}
Yb	0.4115 ^{c,d,e}	1.3495 ^{m,t,u,v,w,x}	Li	0.16 ^b	0.26 ^l

Er	0.566 ^{c,e}	0.8 ^f	Rb	0.13 ^a	0.07686 ^{f,g}
a: Villemant et al. (1981), b: Wood and Trigila (2001), c: Shimizu (1980), d: Zack and Brumm (1998), e: Fujimaki et al. (1984), f: Ronov and Yaroshevskiy (1976), g: Hart and Brooks (1974), h: Reid (1983), i: Dostal et al. (1983), j: Gallahan and Nielsen (1992), k: Ewart et al. (1973), l: Matsui et al. (1977), m: Hauri et al. (1994), n: Beattie (1993), o: Irving and Frey (1984), p: Skulski et al. (1994) q: Brunet and Chazot (2001), r: Baker and Wyllie (1992), s: Jenner et al. (1993), t: Johnson and Kinzler (1989), u: Johnson (1994), v: Hart and Dunn (1993), w: Hack et al. (1994), x: Nicholls and Harris (1980), y: Forsythe et al. (1994). *From l to z the kds are for basaltic melt.					